JOURNAL OF AIRCRAFT
Vol. 47, No. 5, September–October 2010

Computational Fluid Dynamics Analyses of Flow over Weapons-Bay Geometries

S. J. Lawson* and G. N. Barakos†
University of Liverpool, Liverpool, England L63 3GH, United Kingdom

DOI: 10.2514/1.C000218

Detached-eddy simulations for the M219 experimental cavity geometry and the 1303 uninhabited combat air vehicle cavity geometry are presented. First, results from three computations are presented with the aim of studying the effect of imposing synthetic velocity fluctuations at the inflow boundary. Both methods employed (synthetic-eddy method and fluctuations from a precursor large-eddy simulation) increased the high-frequency content in the boundary layer upstream of the cavity. Averaged profiles showed little change in the streamwise velocity; however, the profiles of normal velocity were noticeably different. The influence of the upstream boundary layer on the cavity flowfield means that the full aircraft geometry needed to be modeled. Consequently, advanced multiblock topologies had to be used to properly represent the planform of the uninhabited combat air vehicle and all the details of the cavity, including doors and hinges, while sliding meshes were needed to insert the store into the uninhabited combat air vehicle configuration. Results with an empty cavity were encouraging for such complex configurations. Visualizations using the Q criteria revealed the added turbulent content due to the door leading edges and the door hinges. The addition of a store in between the doors had little effect close to the front wall. However, averaged flowfields showed that the proximity of the shear layer to the apex of the store deflected it downward into the cavity and restricted its growth. Outside the cavity, shedding was observed from the sting and force balance.

I. Introduction

CAVITY flows are encountered in many aerospace applications, the most common being the flow over a weapons bay, and have recently received attention from the computational fluid dynamic (CFD) community due to the challenges they pose for turbulence models. Recent computational works have used large-eddy simulation (LES) [1–3] and detached-eddy simulation (DES) [3–5] to study the viability of using these techniques for the problem. A summary can be found in Lawson and Barakos [5].

For idealized geometries, reasonable agreement with wind-tunnel data is obtained. The acoustical signature in the cavity is composed of two parts: broadband noise and narrowband tones. The broadband is low-energy noise contributed by the freestream, the shear layer, and turbulence. The tones, called Rossiter modes [6], can vary in magnitude and are caused by specific interactions in the flow. Many numerical computations overpredict the overall sound-pressure level (OASPL) along the cavity floor by 3–5 dB, which is usually attributed to an overprediction of the amplitude of the Rossiter modes [5].

For many applications, inflow turbulence can influence the results of unsteady simulations [7]. LES and DNS computations sometimes use turbulent inflow conditions that are synthetically generated, especially those that include wall boundaries. This reduces the cost of a simulation as a shorter inflow domain can be used. Several methods exist for generating a turbulent inflow, including adding random white noise, inverse Fourier methods [8], precursor or parallel simulations [9], the recycling method [10,11], and synthetic-eddy methods [12–15].

Many computational results given in the literature do not use any of the methods above for the inflow condition. Therefore, there may be differences between the computational simulations and experimental tests in how the instantaneous structures in upstream boundary layer seed the shear layer. LES results from Gloerfelt et al. [16] on a cavity with a length L to depth D ratio of 2 at Mach 0.8 found the sound-pressure spectrum levels (SPLs) for a laminar upstream boundary layer to be 3 dB higher than a turbulent one. Chang et al. [17] implemented realistic turbulent inflow conditions on the same cavity and concluded that the upstream velocity fluctuations increased the range of turbulent eddies present in the cavity. Sagaut et al. [7] applied inflow fluctuations to a deep cavity (L/D ratio of 0.42) and showed that at small distances upstream of the cavity, the streamwise (u) and normal (v) components of the velocity were unaffected by the addition of inflow fluctuations. It was concluded this was due to the strong two-dimensional pressure waves traveling upstream from the cavity. Therefore, the inflow condition had little influence on the mean flowfield and the only effect was to make the boundary layer more three-dimensional.

The CFD analysis of the full aircraft geometries with weapons bay exposed and possibly with stores inside presents a formidable task in terms of mesh generation and computation. For this reason, the study of the isolated cavity would be desirable, but only if the obtained results were similar to the real configuration. However, the conflicting views within the literature on the influence of the flow upstream means that to simulate the flow inside the weapons bay of an uninhabited combat air vehicle (UCAV), the full geometry may be needed to gain a realistic solution. Published works on UCAVs and their performance are relatively rare. Wong et al. [18] presented results from The Technical Cooperation Program studying a design designated 1303 UCAV, which resulted in experimental and numerical data. These results showed that the Reynolds-averaged Navier–Stokes equations (coupled with various turbulence closures) gave a reasonable overall prediction for the external flow at modest angles of attack. In a separate study, when a weapons bay was added to the UCAV [19–21], a small overprediction in the OASPL was seen all along the cavity floor compared to experiments by Hill and Lawson [22] and had a maximum of 3 dB at around the midpoint of the cavity.

In view of the above, this paper attempts to obtain a set of numerical results for the cavity flows with the aim of obtaining more favorable comparisons to experimental data. First, results are presented for an ideal cavity geometry with and without turbulent forcing at the domain inlet to determine the extent of the influence of the boundary-layer structure. Then results of computations of a realistic UCAV geometry are presented. It is the view of the authors

Presented as Paper 2010-1425 at the 48th AIAA Aerospace Sciences Meeting, Orlando, FL, 4–7 January 2010; received 5 December 2009; revision received 19 April 2010; accepted for publication 27 April 2010.

*Research Associate, CFD Laboratory, School of Engineering; S.J.Lawson@liverpool.ac.uk.

†Professor, CFD Laboratory, School of Engineering; G.Barakos@Liverpool.ac.uk. Member AIAA (Corresponding Author).

that this is the first time that such calculations have been performed and compared against experimental data.

II. Numerical Methods

A. CFD Flow Solver

The parallel multiblock flow solver of Liverpool has been successfully applied to a variety of problems, including cavity flows, hypersonic film cooling, spiked bodies, flutter, and delta wing flows, among others [23]. The governing equations are the unsteady three-dimensional compressible Navier–Stokes equations, written in dimensionless form as

$$\frac{\partial Q}{\partial t}+\frac{\partial}{\partial x}\left(F^{\text{inv}}+\frac{1}{Re}F^{\text{vis}}\right)+\frac{\partial}{\partial y}\left(G^{\text{inv}}+\frac{1}{Re}G^{\text{vis}}\right)+\frac{\partial}{\partial z}\left(H^{\text{inv}}+\frac{1}{Re}H^{\text{vis}}\right)=\mathbf{S} \tag{1}$$

where Q contains the unsteady terms and F, G and H are spatial flux vectors and have been split into their inviscid (inv) and viscous (vis) parts. The source vector is denoted by $\mathbf{S}$.

The code solves the governing equations on multiblock structured grids using a cell-centered finite volume method. The convective terms are discretised using either the Osher–Chakravarthy [24] or Roe [25] approximate Riemann solvers. MUSCL interpolation [26] is used to provide formally third-order accuracy and the van Albada limiter is used to avoid spurious oscillations across shocks. The time-marching of the solution is based on the implicit dual-time-stepping method of Jameson [27]. The final algebraic system of equations is solved using the generalized conjugate residual method [28], in conjunction with block incomplete lower–upper factorization. A number of turbulence models, including one- and two-equation statistical models as well as LES and DES formulations, have been implemented into the code. More details of the employed CFD solver and turbulence models are given in Nayyar et al. [3].

B. Postprocessing Methods

The power spectral density (PSD), OASPL, and band-integrated sound-pressure level (BISPL) provide a means of comparing the numerical results to the experimental unsteady pressure data along the cavity floor. The PSD is used to study the frequency content of a signal at a given location and is based upon the unsteady pressure p', where $p'=p-\bar{p}$. The PSD was calculated using the Burg estimator [29] (also known as maximum-entropy method), as it produces better resolved peaks for short signals than traditional fast Fourier transforms [2]. For a description of the PSD in terms of decibels, the natural definition is that of the sound-pressure spectrum level [30]:

$$\text{SPL}\,(f)=10\text{LOG}_{10}\left[\frac{\text{PSD}(f)\,\Delta f_{\text{ref}}}{p_{\text{ref}}^2}\right] \tag{2}$$

where Δf_{ref} is a reference frequency, usually set to 1 Hz, and p_{ref} is the international standard for the minimum audible sound, which has the value of 2×10^{-5} Pa [30].

The variation in pressure levels along the cavity floor was studied using the rms of the unsteady pressure, p'_{rms}, and can be obtained from the measurements using the following equation:

$$p'_{\text{rms}}=\sqrt{\frac{1}{N}\sum(p')^2} \tag{3}$$

Although p'_{rms} is measured in pascals (or any other unit of pressure), it is customary in cavity flow studies to report it as the OASPL [30]:

$$\text{OASPL}\;=20\,\text{LOG}_{10}\left[\frac{p'_{\text{rms}}}{p_{\text{ref}}}\right] \tag{4}$$

which has the units of decibels. BISPL plots show the energy content within a particular frequency range and is calculated using the following equation:

$$\text{BISPL}\;=20\,\text{LOG}_{10}\left[\left(\int_{f_1}^{f_2}\text{PSD}(f)\right)^{1/2}\cdot\frac{1}{p_{\text{ref}}}\right] \tag{5}$$

where f_1 and f_2 are the lower and upper limits of the desired frequency range. Although the magnitude of the BISPL aids in identifying which frequencies are significant, the shape of each banded mode is also important as it represents how each frequency band varies along the cavity length. For cavity flow studies, the BISPL plots are usually centered around the first four Rossiter modes [6].

Comparisons of numerical data to experimental data for an unsteady flow is not a simple one. In particular for cavity flows, a mode switching phenomenon occurs [4]. Therefore, in processing the experimental data, it is split into segments equalling the length of the numerical signal, with each segment having a 90% overlap. Each segment is then processed using the methods given above and at each location the maximum and minimum levels in the OASPL and BISPL are recorded. These are represented on the plots by error bars. The curve plotted in the PSD is the segment deemed to be the best fit to the numerical data, where the metric used to define the best fit was the OASPL. Note that the maximum or minimum limits may not be from the same segments of data. Therefore, the segment used to plot the PSD is also plotted in the OASPL and BISPL to give a reference of how the shape varies along the length. This segment will therefore not necessarily lie in the center of the error bars.

The tones in the PSD are usually termed Rossiter modes [6] and a semi-empirical formula is available for the estimation of their frequencies. Rossiter based the formula on experimental results over a range of Mach numbers from 0.4 to 1.4 and on various cavity aspect ratios. However, outside this range the accuracy of the predictions decreases and so Heller et al. [31] modified the original formula to compensate. The modified version is as follows:

$$f_m=\frac{U_\infty}{L}\left[\frac{m-\alpha}{M_\infty(1+[(\gamma-1)/2]M_\infty^2)^{-1/2}+1/\kappa_v}\right] \tag{6}$$

where f_m is the frequency of mode m, U_∞ and M_∞ is the freestream velocity and Mach number, respectively, and L is the cavity length. γ is the ratio of specific heats, α represents a phase shift and κ_v is a constant dependant on the cavity geometry and test conditions. These constants have the values 1.4, 0.25 and 0.57, respectively. The formula is used here for comparisons with CFD results.

Experimental studies of mixing layers found that close to the origin there was a dependence on the speed ratio λ, which is defined as $\lambda=\Delta U/2\bar{U}$, where ΔU is the difference in velocity between the two fluids (for a cavity, λ has the values of 1.0). However, after a distance $\lambda x/\delta_m^0\approx400$–$500$, the results followed a single linear growth rate [32]. Values for the gradient $(\mathrm{d}\delta_m/\mathrm{d}x)$ range between 0.03 and 0.04 [2]. Studying data from difference speed ratios, Browand and Troutt [32] found a value of 0.034λ. Huang and Ho [33] found similar values, even if the mixing layer was forced at a different frequency. The LES computation from Larchevêque et al. [2] gave a value of 0.035. Here, as with other studies, the incompressible definition is used and the influence of the recirculation region is neglected [2]. Therefore, the momentum thickness is defined as

$$\delta_m(x,z)=\int_{y_0(x,z)}^{\infty}\frac{u(x,y,z)}{U_\infty}\left[1-\frac{u(x,y,z)}{U_\infty}\right]\mathrm{d}y \tag{7}$$

where $y_0(x,z)$ is the y location, and $u(x,y,z)\equiv0$.

Turbulent structures are inherently three-dimensional and so to better identify them within the flow, the Q criteria is used. Hunt et al. [34] proposed the Q criteria to identify vortex cores and reflects the amount of strain and vortical motions in a vector field. Let ∇u denote the gradient of the velocity field. The Q criteria is then defined as the positive second invariant of the velocity gradient tensor:

$$Q\equiv\tfrac{1}{2}(u_{i,i}^2-u_{i,j}u_{j,i})=-\tfrac{1}{2}(u_{i,j}u_{j,i})=\tfrac{1}{2}(\|\mathbf{\Omega}\|^2-\|\mathbf{S}\|^2) \tag{8}$$

where $\mathbf{S}$ and $\mathbf{\Omega}$ are the symmetric and antisymmetric components of ∇u. The strain tensor is defined as the symmetric part and the antisymmetric part is closely related to the vorticity. Thus, the Q

criteria represents the local balance between shear strain rate and vorticity magnitude [35]. When $Q > 0$, vorticity dominates strain and so identifies a vortex region.

III. Ideal Cavity Computations

The authors have carried out numerous computations on idealized cavity flows with unsteady Reynolds-averaged Navier–Stokes (URANS) and DES using the multiblock solver of Liverpool [4,5,36–38] and are discussed in the following sections.

A. Results of Unforced Simulations

DES results for ideal cavities (Fig. 1) were compared with the M219 cavity experimental data from Nightingale et al. [39], where it was shown that the OASPL was within 5 dB all along the cavity floor for all cases presented [5]. The agreement was found to improve with mesh size and signal length. Figure 2 presents the results for the clean cavity (i.e., no flow control devices attached) with bay doors using the Spalart–Allmaras (S-A) DES model [40]. The PSD (Fig. 2a) shows that the frequency and magnitude of the second tone were predicted well, with the magnitude of the fourth mode being slightly overpredicted. Also the level of the broadband noise was similar to the experimental data.

The OASPL (Fig. 2b) includes points on the cavity floor ($y/L = -0.2$ where $x/L > 0$) and on the plate ahead of the cavity ($y/L = 0$ where $x/L < 0$). It shows that the magnitude of the pressure fluctuations was generally overpredicted, although the overprediction was relatively constant along the whole length of the cavity, as also seen in other studies [5]. The similarity of the numerical and experimental curves suggests that the flow structures inside the cavity were well predicted by the DES model. The averaged flowfield shows a small recirculation region in the lower front corner; however, toward the rear of the cavity, the primary vortex filled most of the cavity volume. Further results for clean cavities and cavity with passive flow control devices can be found in [4,5,36–38].

Although the OASPL data on the cavity floor shows good agreement with experiments, PSD plots for locations ahead of the cavity show that the numerical data does not have the correct frequency content. Figure 3 shows the PSD for locations $x/L = -0.35$ and $x/L = -0.2$ ahead of the cavity (where $x/L = 0$ corresponds to the cavity leading edge) for the doors-on clean-cavity configuration. Both plots showed a lack of content above a frequency of 500 Hz. The plots also show an overpredicted second mode, especially at $x/L = -0.35$, where the mode in the experimental data was only about 5 dB above the broadband level and had a magnitude of approximately 115 dB. In the numerical data, the second mode was about 30 dB above the broadband noise level and had a magnitude of 130 dB. In summary, the boundary layer upstream of the cavity did not contain the correct frequency content.

B. Inflow Forcing

For the unforced cavity computations, the flow variables at the inflow boundary were set to freestream conditions and a nominal amount of eddy viscosity was prescribed which corresponded to the freestream levels of turbulence in the experimental tests. Also. in the DES formulation, the boundary layer was resolved using URANS and so contained no instantaneous turbulent structures. Therefore, it was decided to impose some artificial fluctuations at the inflow to energize the boundary layer. The precursor LES simulation and the synthetic-eddy method (SEM) were chosen to assess the differences the boundary structure has on the cavity dynamics.

1. *Precursor LES Simulation*

An LES simulation was performed for a channel flow at a Mach number of 0.5 using a separate fourth-order finite difference code developed to produce inflow fluctuations. To gain the LES data with reasonable computational cost, the Reynolds number of the calculation was set to 20,000 based on half the height of the channel (H). The computations used a regular mesh of approximately 185,000 cells, where the domain extended $1.3H$, $1.0H$, and $1.0H$ in the streamwise, normal and spanwise directions, respectively. A no-slip condition was imposed on the solid surface, while in the spanwise direction periodic conditions were used. The upper surface in the normal direction was given a symmetry condition. The flow through the outflow boundary was recycled and used as inflow.

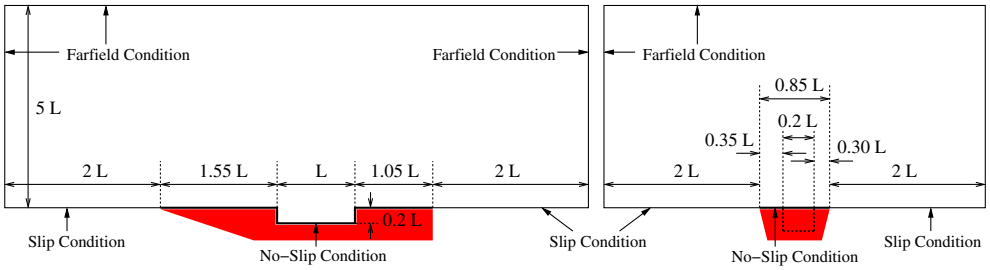

Fig. 1 Geometry and boundary conditions for the M219 cavity computations.

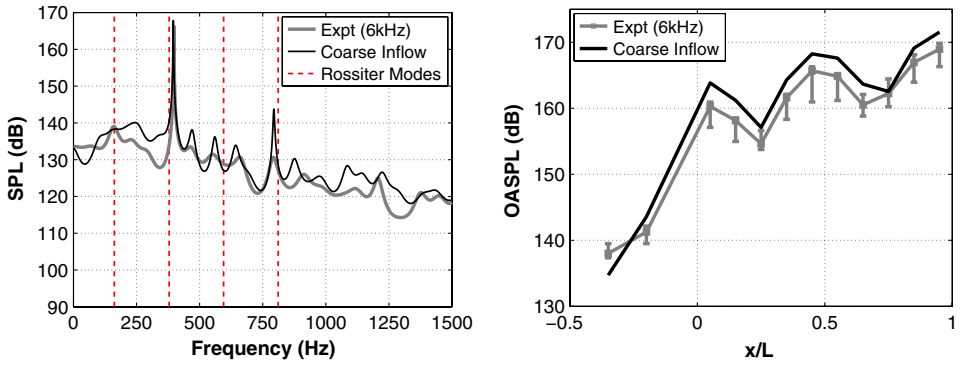

a) PSD **b) OASPL**

Fig. 2 Plots of a) PSD and b) OASPL for the M219 clean cavity with doors-on comparing results from DES computations to the M219 experimental data from Nightingale et al. [39]. PSD plot is at $x/L = 0.95$ on the cavity floor and presented in terms of SPL. The error bars in the OASPL denote minimum and maximum values from the different sections of the experimental data.

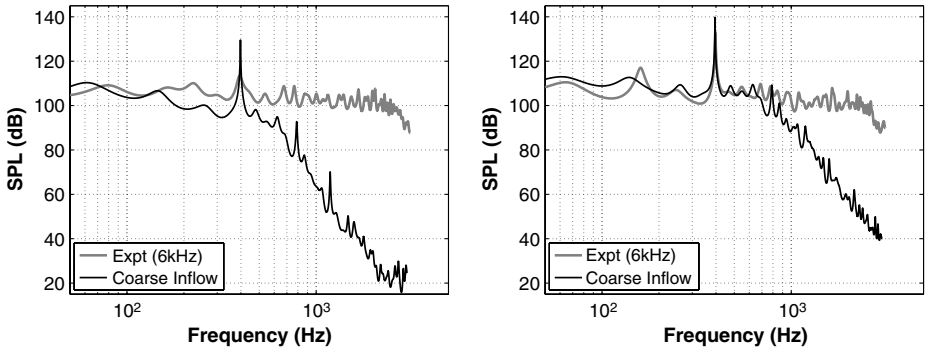

Fig. 3 PSD plots for the M219 clean cavity with doors-on comparing results from computations to the M219 experimental data from Nightingale et al. [39] for two locations upstream of the cavity, presented in terms of SPL.

The code was run for 50,000 time steps, with slices taken at the center of the domain (in the streamwise direction) for the final 10,000 steps. The mean (using 40,000 steps) was then extracted and the fluctuations were interpolated (in both space and time) onto the inflow domain of the cavity grid at each time step of the cavity simulation. The data were stored in one file per block and read into memory at the beginning of the cavity computation.

2. Synthetic-Eddy Inflow Method

The SEM used here was proposed by Jarrin et al. [13,14] and is based on the classical view that turbulence is a superposition of coherent structures. The velocity fluctuations are generated over the inlet through turbulent spots. Each turbulent spot k has a location x_j, a length scale σ_j, and a sign ε_j. The contribution to the velocity field u_i from each spot is estimated by

$$u_i^k(x_j) = \varepsilon_i^k f_{\sigma_j}(x_j - x_j^k) \tag{9}$$

where f_{σ_j} is a symmetric shape function that characterizes the decay of the fluctuations generated by each turbulent spot. The employed shape function was

$$f_{\sigma_j}(r) = \sqrt{\frac{3}{2\sigma}}\left(1 - \left|\frac{r}{\sigma_j}\right|\right) \tag{10}$$

The velocity fluctuations at point x is the sum of the contributions from all the turbulent spots:

$$u_i'(x_j, t) = \sqrt{\frac{1}{N}}\sum_{k=1}^{N} \varepsilon_i^k f_{\sigma_1}(x_1 - x_1^k(t)) f_{\sigma_2}(x_2 - x_2^k(t)) \times f_{\sigma_3}(x_3 - x_3^k(t)) \tag{11}$$

The turbulent spots are randomly generated on $[-\sigma_x, \sigma_x] \times [-\sigma_y, L_y + \sigma_y] \times [-\sigma_z, L_z + \sigma_z]$ and are convected through the inlet plane with reference velocity U_0 using Taylor's frozen turbulence hypothesis:

$$x^k(t + \mathrm{d}t) = x^k(t) + U_0 \mathrm{d}t \tag{12}$$

When a turbulent spot reaches the end of the domain ($x^k > \sigma_x$), it is regenerated upstream at $x^k = -\sigma_x$. The position in the normal (y) and spanwise (z) directions are randomly generated, along with the sign ε_j. The method was added to the existing CFD solver as an addition boundary condition and so performs the additional calculations at run time.

C. Details of the Computations

To preserve the velocity fluctuations imposed at the inflow, the mesh upstream needed DNS scale resolution and so would increase the size of the mesh dramatically. Therefore, to conserve grid cells, a mesh for a quasi-3-D (Q3D) geometry was designed. The domain of the grid, based on the M219 cavity geometry [39], was reduced to a slice of width $0.5D$. The sides of the domain were given a symmetry boundary condition. The first cell size in the normal direction (Δy_1) was set to $10^{-4}L$. 40 cells with equal spacing were used in the spanwise direction, which gave a maximum cell spacing of $2.5\times 10^{-3}L$, or $25\Delta y_1$. To match the spacing in the cavity, 540 cells were used in the streamwise direction and 160 in the normal direction, giving a total of 3.5 million cells inside the cavity.

The plate ahead of the cavity had a length of $1.55L$, which needed 3120 cells in the streamwise direction to maintain a maximum spacing of $5 \times 10^{-4}L$ ($5\Delta y_1$). In the normal direction, 40 cells were used between the plate and $0.01L$ above the surface, where the cells were stretched from $10^{-4}L$ to $5 \times 10^{-4}L$ using a hyperbolic distribution. This meant that the cells in the boundary layer remained relatively orthogonal. Above the first layer of 40 cells, another 40 cells were used to the far field, which extended $3L$ above the plate. 120 cells were used to describe the plate behind the cavity, which had a length of $1.05L$, which gave the cells a maximum spacing of $0.025L$. In total, the grid for the quasi-3-D cavity contained 16.8 million cells.

Three computations were performed: one with no inflow (NI) fluctuations, one with SEM imposed at the inflow boundary, and one with the LES fluctuations applied at the inflow. The approach for the computations with the inflow forcing is termed stimulated DES [41]. All the computations used the DES S-A model [40] and were performed at Mach and Reynolds numbers of 0.85 and 1×10^6. A dimensionless time step of 1×10^{-3} was used for all computations; therefore, 1000 time steps correspond to the time it takes a particle to travel the length of the cavity in the freestream flow. The computation without any inflow fluctuations was initially ran for 15,000 time steps, which based on previous experience was adequate to create a fully developed turbulent flowfield. This solution was then stored and used as the starting point for all three computations. Once the inflow boundary conditions were imposed, the computations were ran for a further 10,000 time steps to allow the synthetic fluctuations to influence the flowfield. Data were then recorded from time steps 25,000 to 35,000. Although the sampling time was relatively short compared to the other cavity computations performed, it was long enough to assess the methods employed. Probe data were sampled at every time step, while flowfield data were stored every 100 time steps, which equated to a sampling frequency of approximately 5500 Hz. Note that the imposed fluctuations did not affect the profile of the boundary layer in the averaged flowfields.

D. Results of Forced Simulations

The pressure fluctuations at the inlet are shown in Fig. 4a and the corresponding frequency spectrum is shown in Fig. 4b. The computation with no inflow showed a slow oscillation in the pressure trace, which gave a large tone at around 180 Hz and a smaller tone at around 350 Hz. However, the signal contained little content at higher frequencies. With the inflow fluctuations applied, both the SEM and LES computations exhibited high-frequency oscillations. Compared to the NI computation, the tones occurred at slightly higher

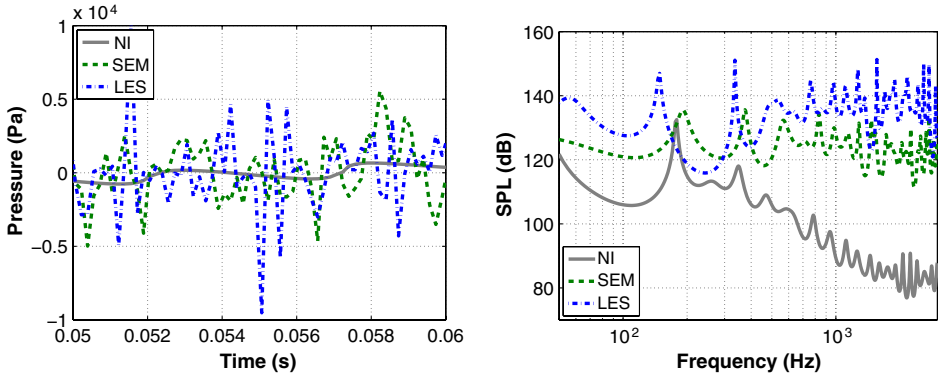

a) Time trace b) PSD

Fig. 4 Plots of a) time trace and b) PSD for the Q3D cavity at the inflow ($x/L = -1.69$) comparing results from the computation with no inflow fluctuations (NI), SEM imposed at the inflow (SEM), and fluctuations extracted from a precursor LES simulation (LES). For clarity, the LES data has been offset by adding 10 dB. The PSD is presented in terms of SPL.

frequencies for the SEM computation and at slightly lower frequencies for the LES.

Pressure spectra at distances of $0.35L$ and $0.2L$ ahead of the cavity are shown in Fig. 5, which are the same positions shown in Fig. 3 for the M219 clean-cavity computation. Along with the Q3D NI, SEM, and LES results, the experimental data for the M219 clean cavity with doors is also shown. First, the Q3D cavity had different characteristics to the M219 cavity. The low-frequency part of the signal had a much higher magnitude and thus the first mode was larger than any other mode. However, the magnitude of the high-frequency part of the signal (above about 800 Hz) still falls off similar to the M219 cavity when compared to the experimental data (as shown in Fig. 3). Second, the two inflow methods affected the signal in slightly different ways. The LES inflow data added some content at frequencies above 2 kHz, while having a relatively small effect on the lower frequency range. At both locations, the first mode had a slightly higher magnitude, while in the second plot the second mode shifted to a lower frequency. The SEM had a much larger effect on the signal than LES inflow data. Much more high-frequency content was added at frequencies above 1 kHz and the modes also had slightly higher magnitude.

The effect of reducing the width of the computational domain was very evident in the spectra upstream of the cavity. It was shown in the clean-cavity results that when the doors were attached, they channelled the flow and so the pressure waves propagated upstream had larger fluctuations than if the doors were not attached [4]. Here, with the whole domain reduced to the cavity width, the pressure waves traveling upstream modulate the pressure fluctuations as far upstream as the inflow plane (Fig. 4b).

Figures 6 and 7 show the effect of the forced inflow on signals on the cavity floor. PSD plots at the front and rear of the cavity revealed that although the domain was reduced to the width of the cavity, the spectral pattern for the NI case did not resemble the doors-on clean cavity (where a single peak for the second Rossiter mode dominated). Instead, it resembled the multiple peak spectra of the doors-off case.

The addition of the inflow forcing increased the magnitude of the first mode at both locations, but also decreased the second mode, with the LES inflow having the larger influence. The effect along the cavity floor can be seen in Fig. 7a, where the shape of the OASPL changed from a W shape (which was actually similar to the M219 clean-cavity doors-on data, despite the existence of multiple peaks) to a V shape. Surprisingly, the OASPLs for the two computations with inflow forcing were almost identical, with the only difference occurring close to the front of the cavity.

The BISPL plots for the first three modes are shown in Figs. 7b and 7d. These revealed the cause of the change in the OASPL when using the inflow conditions, as the magnitude of the first mode was increased almost all along the cavity floor, while the second mode was decreased. The SEM computation also increased the third mode at the front of the cavity, which was consistent with the earlier observation that the SEM added more higher frequency content. However, further down the cavity, this extra energy was dissipated by the shear layer and so had similar levels to the other computations.

The reduction of the second mode is encouraging and suggests that the addition of velocity fluctuations at the inlet influences the flow and reduces the amplitude of the highest-amplitude modes. The increase of the first mode was overlooked here, since it appeared that this mode was amplified greatly by the reduced computational domain.

1. *Instantaneous and Averaged Flowfields*

The influence of the fluctuations on the creation of small scale structures is shown in Fig. 8, which presents instantaneous isosurfaces of Q criteria for the computations. The levels of Q shown pick up the vortex cores inside the cavity, but are not low enough to

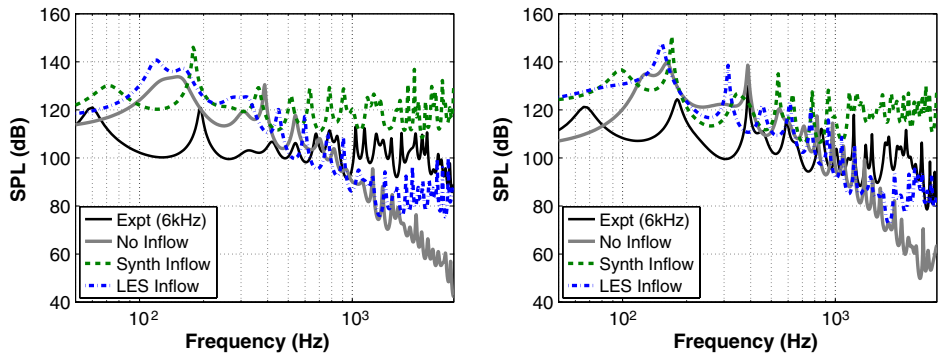

a) $x/L = -0.35$ b) $x/L = -0.2$

Fig. 5 PSD plots for the Q3D cavity comparing results from the NI, SEM, and LES computations to the M219 experimental data from Nightingale et al. [39] for the clean-cavity doors-on configuration. Plots are for two locations upstream of the cavity and presented in terms of SPL.

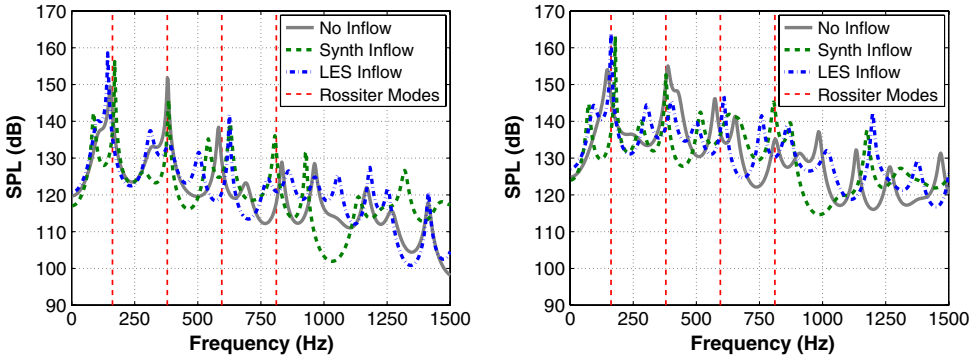

a) $x/L = 0.05$ b) $x/L = 0.95$

Fig. 6 PSD plots for the Q3D cavity comparing results from the NI, SEM, and LES computations: a) front and b) rear transducers on the cavity floor, presented in terms of SPL.

identify the structures in the upstream boundary layer. Comparing the three computations, the flow was more three-dimensional with the fluctuations added, which was especially evident close to the front edge of the cavity in the SEM computation.

Comparing the current findings to those of other studies, Sagaut et al. [7] concluded that the actual structure in the upstream boundary layer was not important. This was a result of the main cavity mechanism being two-dimensional and so the upstream pressure fluctuations were dominated by the reflected pressure waves. This can be seen in the PSD spectra of both the M219 cavity and the Q3D cavity computations. Lin and Rockwell [42] found that values of the cross Reynolds stress in the shear layer were much larger that the values found in the turbulent boundary layer and so suggested a dominance of the shear-layer dynamics. However, it was identified that additional mechanisms may exist relating to a small scale instability resulting from the hairpin vortices in the boundary layer. The visualization of Q tends to agree that the structure does make a difference. Not only can more structure be seen close to the leading edge, but the size of the structures was also altered. The NI computation exhibited quite large structures, especially toward the rear, whereas the SEM and LES computations seemed to contain much smaller structures.

Averaged profiles for the streamwise velocity, the normal velocity and the turbulent kinetic energy are shown in Fig. 9. The profiles showed that the streamwise component was little affected by the inflow fluctuations, with only small differences in the profiles near the cavity floor. Although there were noticeable differences in the normal component in the aft half of the cavity, some of the differences could be due to the relatively short averaging time (only 100 instantaneous flowfields were used). The profiles of turbulent kinetic energy showed similar levels inside the cavity between the three computations, although again the main differences occurred close to the floor in the aft part of the cavity.

Contours of OASPL are shown in Fig. 10 for the three computations. It was discussed previously that the PSD spectra for the NI computation resembled the M219 doors-off cavity case, whereas the OASPL along the floor resembled the doors-on case. Here, the flowfield for the NI simulation again resembled the

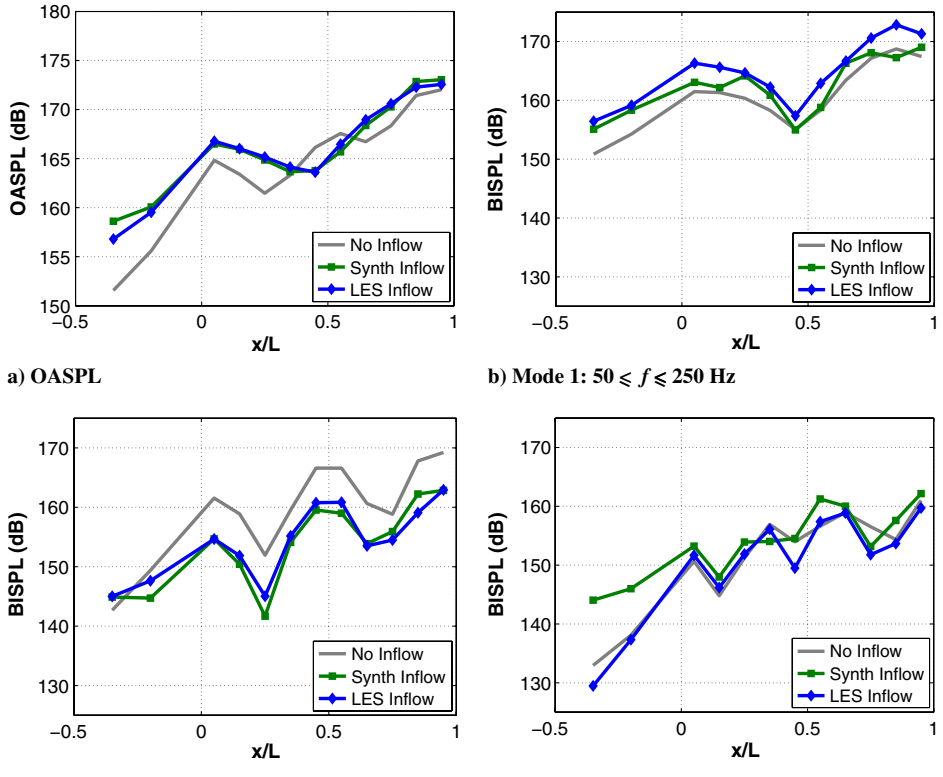

a) OASPL b) Mode 1: $50 \leqslant f \leqslant 250$ Hz

c) Mode 2: $250 \leqslant f \leqslant 450$ Hz d) Mode 3: $500 \leqslant f \leqslant 700$ Hz

Fig. 7 Plots of a) OASPL and b–d) BISPL along the cavity floor for the Q3D cavity comparing results from the NI, SEM, and LES computations.

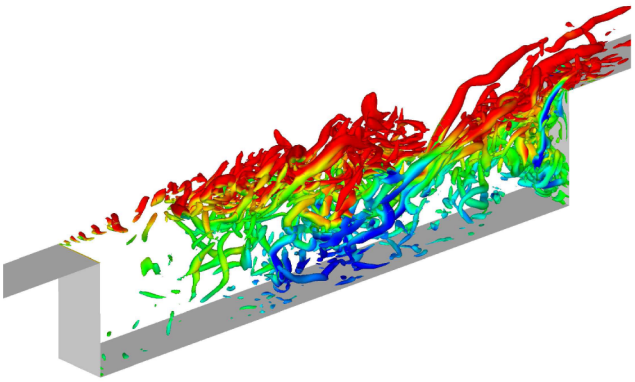

a) NI

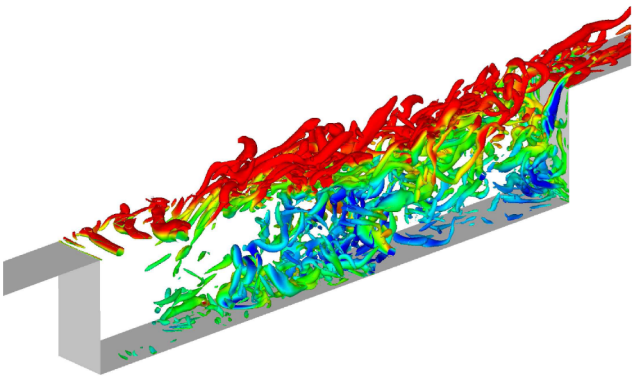

b) SEM

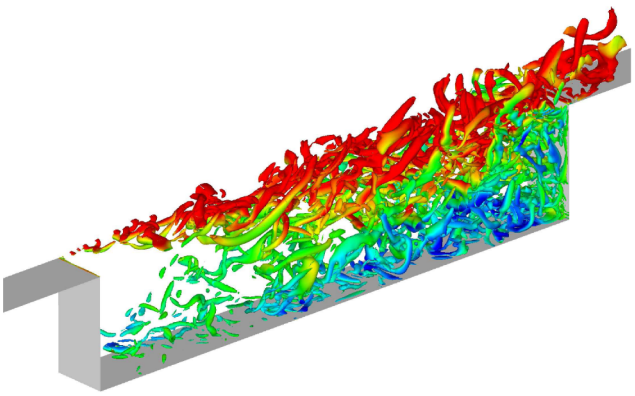

c) LES

Fig. 8 Instantaneous isosurfaces of Q criteria for the Q3D cavity comparing results from the a) NI, b) SEM, and c) LES computations. Isosurfaces at $Q = 2000$ are shown and shaded with dimensionless streamwise velocity, ranging between -0.5 and $+0.5$.

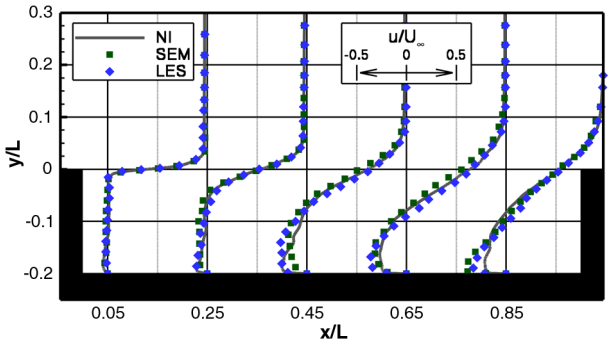

a) u velocity

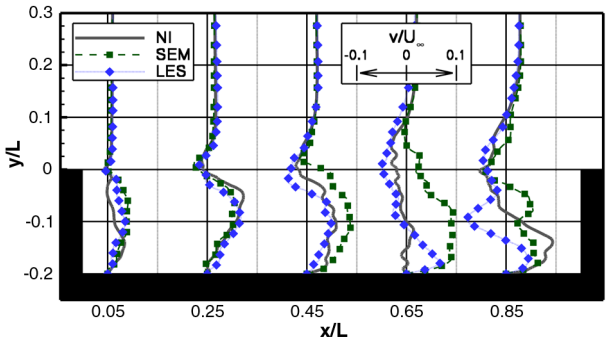

b) v velocity

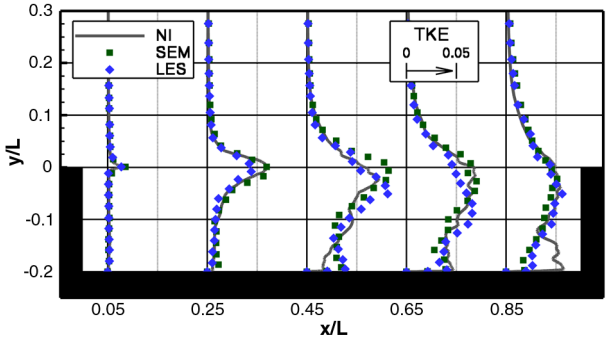

c) Turbulent kinetic energy

Fig. 9 Averaged profiles for the a) streamwise velocity, b) normal velocity, and c) turbulent kinetic energy at the cavity centerline ($z/L = 0.05$). Results shown compare NI, SEM, and LES computations.

doors-off case. The shear layer and aft wall were surrounded by area of high OASPL, while an area in the bottom front corner had lower OASPL. The flowfields with inflow conditions were very similar, where the small area of high OASPL at the front corner extended down to the cavity floor and the noise propagated into the far field was increased. The fluctuations in the SEM computation caused higher OASPL upstream of the cavity and also behind the cavity in the far field as observed in the velocity dilatation flowfields. For the LES, there was a reduction of OASPL in the middle of the shear layer and so high OASPL only occurred near the downstream wall. This may suggest a different shear-layer structure.

2. *Shear-Layer Analysis*

The momentum thickness along the shear layer of the averaged flowfield was calculated and presented in Fig. 11. Here, all three of the computations had similar profiles along the length, with the main section of the curve having a gradient of 0.031. Therefore, the imposed fluctuations seemed to have little effect on the spread rate, which agrees with the conclusion of Huang and Ho [33]. In the rear of the cavity, the behavior for the NI computation was similar to the doors-on clean-cavity configuration, where the gradient decreased [4]. However, the forced computations had a larger thickness as a result of increased mixing and frequency content.

The effect of the inflow conditions on the shear layer can be seen in Figs. 12 and 13. At the front of the cavity (Fig. 12a) the LES inflow increased the magnitude of the first mode and decreased the second. The SEM increased the first mode's frequency and magnitude, slightly decreased the second mode and also added content at frequencies above 1 kHz. At the rear of the cavity, the same trends were observed, with the exception that the content at higher frequencies was comparable for all three cases.

The OASPL and BISPL along the shear layer for the three cases (Fig. 13a) revealed the same pattern as along the cavity floor. The OASPL was significantly altered in the front half of the cavity by the forcing and was the result of an increase in the first mode and a reduction in the second mode. The third mode was slightly increased by the SEM, but slightly decreased by the LES. The BISPL plots for

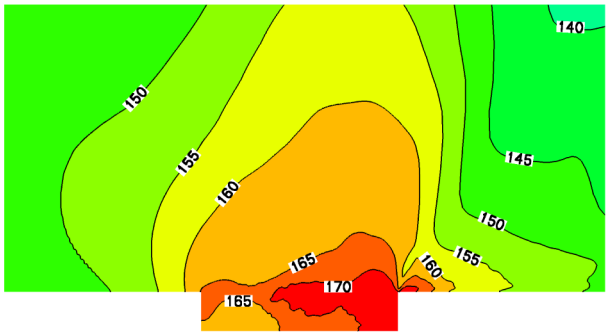

a) NI

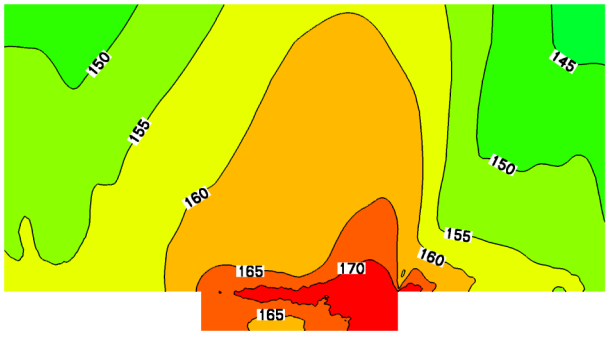

b) SEM

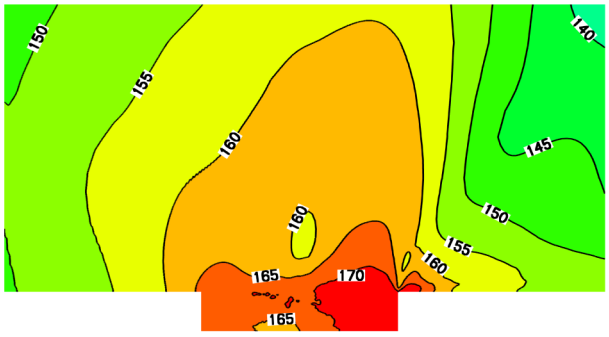

c) LES

Fig. 10 Contours of OASPL at the cavity centerline ($z/L = 0.05$) for the 1) Q3D NI, b) SEM, and c) LES computations.

modes 1 and 2 show that the LES increased the first mode and decreased the second mode more than the SEM.

Figures 13e and 13f show the BISPL for the Rossiter mode and broadband noise contributions, respectively. As in the OASPL plot, the shape of the plot showing the contribution from the Rossiter modes was changed by the SEM and LES fluctuations, especially in the front part of the cavity. As expected, the SEM had a higher contribution from the broadband noise at the leading edge of the cavity. However, further downstream where the dynamics of the shear layer were dominant, the contributions were similar from all three simulations.

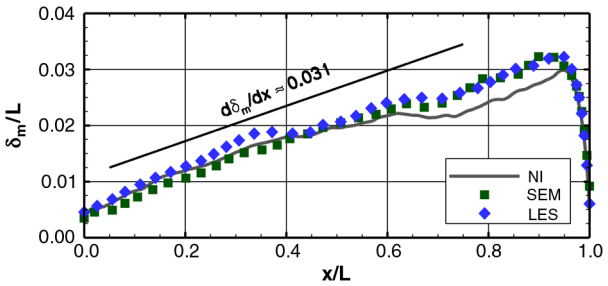

Fig. 11 Momentum thickness of the shear layer of the averaged Q3D NI, SEM, and LES cavity computations. Momentum thickness is nondimensionalized by the cavity length.

IV. UCAV with Weapons Bay

The influence of the upstream flow means that to obtain more realistic predictions for weapons bay flow, the whole aircraft geometry should be modeled. Here, a UCAV geometry designated 1303, was used as experiments were performed with weapons bay exposed and also with stores at various positions.

The geometry for the 1303 UCAV was modeled on the wind-tunnel experiments by Bruce and Mundell [43] and are detailed in Wong et al. [18]. For the CFD computations, the geometry was nondimensionalized by the maximum wing chord length c. The far-field boundaries were then located at a distance of $15c$ away from the model in all three directions. The weapons bay had a length of approximately 0.25 m and a depth of 0.046 m, giving an L/D ratio of 5.45. The width was approximately 0.06 m, yielding a W/D ratio of 1.32. These dimensions are only approximate as the opening of the bay followed the lower surface of the UCAV, which meant that the cross section was not orthogonal. In fact, the bay was not symmetric about any axis line. The store studied in conjunction with the weapons bay was of a generic type. Computations for the UCAV without a weapons bay and the mesh generation for the empty-cavity configuration are presented in previous works by Lawson and Barakos [19–21].

A. Empty Weapons Bay

The computation for the UCAV with cavity was performed at Mach and Reynolds numbers of 0.85 and 10.375 million per meter, respectively, and used DES with the S-A [40] turbulence model. The computations used a time step of 3.14×10^{-6} s, which equated to a frequency of 318 kHz and was then down-sampled to match the sampling frequency of the experimental data. The total runtime of the computation was 0.1 s, where the first 0.02 s were discarded and so gave approximately 0.08 s of data. This signal length is equivalent to over 25 periods of the first Rossiter mode (calculated using Rossiter's formula [6]).

Figure 14a shows the PSD on the cavity floor near the aft wall. The largest tone can be seen at a frequency slightly higher than the prediction of the second Rossiter mode. There was a slight peak around the first mode but no tones can be seen above the broadband level for the third or fourth modes. This trend is similar to the idealized cavity case with doors attached, although in that case a tone around the third mode was seen [4]. In comparison to the experimental data, the frequencies and magnitudes of the first two tones were predicted well. The peak level of the second mode was within 2 dB of the experimental data at all locations along the cavity floor. The general level of the broadband noise was also predicted well, although a slight overprediction can be seen toward the rear of the cavity.

The OASPL across the cavity floor was computed and is shown in Fig. 14b. As the experimental data were shortened to the numerical signal length, the minimum and maximum fluctuations in the full signal are represented by the error bars. A small overprediction all the way along the cavity floor can be seen in the OASPL. The overprediction has a maximum of 3 dB at around the midpoint of the cavity. This is consistent with other computations for idealized cavity flows, where overpredictions as high as 5 dB are reported [5]. Also the error bars on Fig. 14b show that the fluctuations in the experimental data are as high as 5 dB. It is therefore more important that the shape of the OASPL curve is consistent with the experimental data, as this shows that the flow structures captured by the computations are similar to those in the experiments. This is the case for the results shown in Fig. 14b.

To see how the flowfield varies with time, joint time-frequency analysis (JTFA) is used. It has been shown that mode switching occurs in idealized cavity flows [2,4,44]. This is where energy switches between modes and so negates the concept of a single

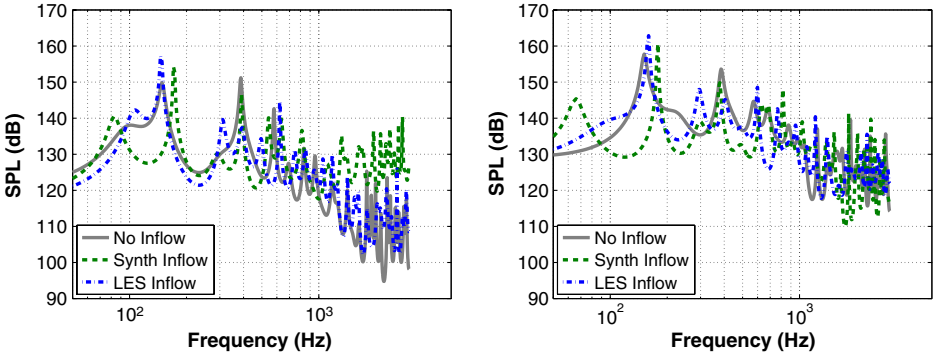

a) $x/L = 0.05$ b) $x/L = 0.95$

Fig. 12 PSD plots for the Q3D cavity comparing results from the NI, SEM, and LES computations: a) front and b) rear transducers along the shear layer, presented in terms of SPL.

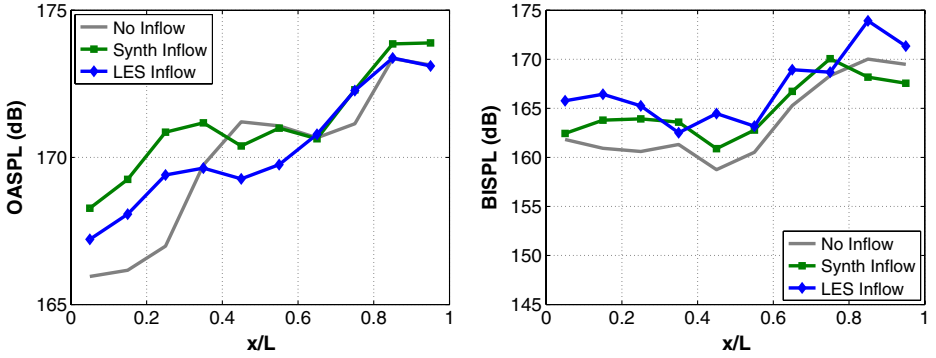

a) OASPL b) Mode 1: $50 \leqslant f \leqslant 250$ Hz

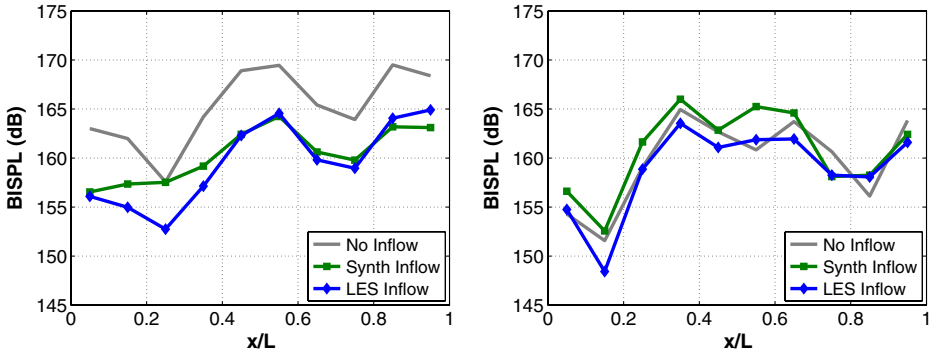

c) Mode 2: $250 \leqslant f \leqslant 450$ Hz d) Mode 3: $500 \leqslant f \leqslant 700$ Hz

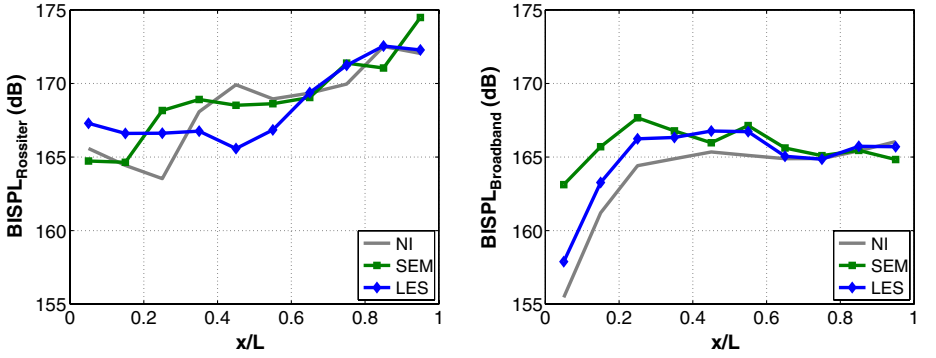

e) Rossiter contribution f) Broadband contribution

Fig. 13 Plots of a) OASPL b–f) BISPL along the shear layer for the Q3D cavity comparing results from the NI, SEM, and LES computations.

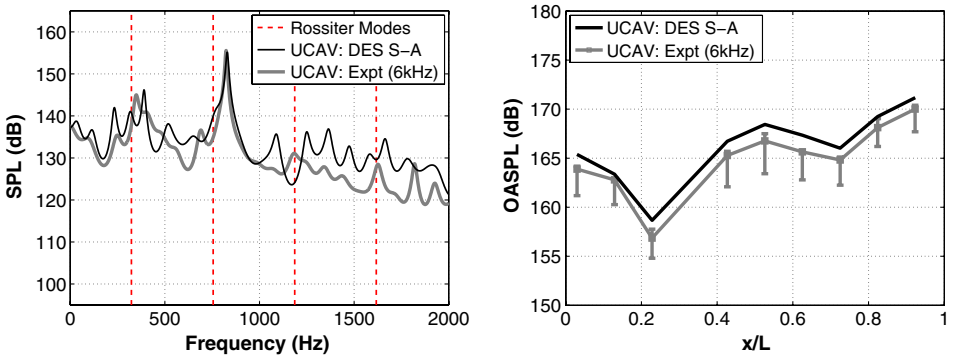

a) PSD at cavity rear b) OASPL

Fig. 14 PSD and OASPL plots for the UCAV with an empty cavity comparing results from computations to the experimental data from Hill and Lawson [22]. PSD plots are for the rear transducers on the cavity floor and presented in terms of SPL. The error bars in the OASPL denote minimum and maximum values from the different sections of the experimental data.

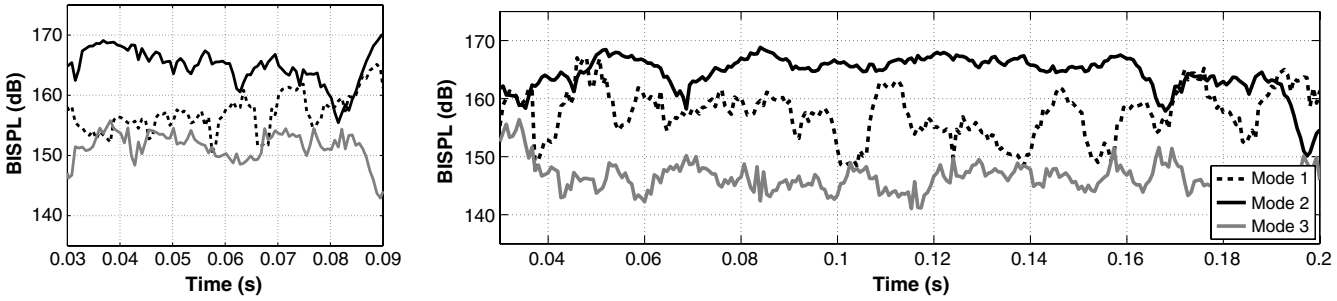

a) DES b) Experiment

Fig. 15 JTFA for the empty UCAV cavity comparing a) numerical results to the b) experimental data from Hill and Lawson [22]. Plots are for the rear transducer at $x/L = 0.92$ on the cavity floor.

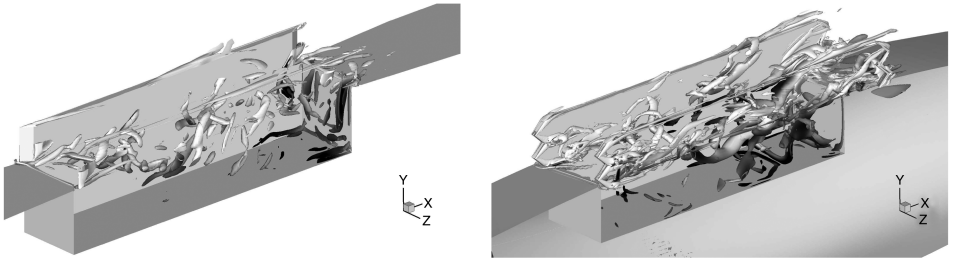

a) Ideal cavity b) UCAV cavity

Fig. 16 Instantaneous isosurfaces of Q criteria for the 1) M219 cavity and b) empty UCAV cavity. Isosurfaces at $Q = 2000$ are shown and shaded with streamwise velocity (nondimensionalized with respect to the freestream velocity), where levels are between -0.5 (black) and $+0.5$ (white).

dominant mode. From the OASPL, it can be seen that fluctuations still occur; however, in this flow the second tone is much larger in magnitude than any other. Figure 15 shows that in both the numerical and experimental data there were few instances in which the second mode was not the largest in magnitude.

As no experimental flowfield data were available for the UCAV cases, the numerical flowfield data were compared to the idealized M219 cavity with doors-on data [3,4]. This cavity had a length to depth ratio of 5 and a width to depth ratio of 1 and like the current study, the freestream Mach number was 0.85, although the Reynolds

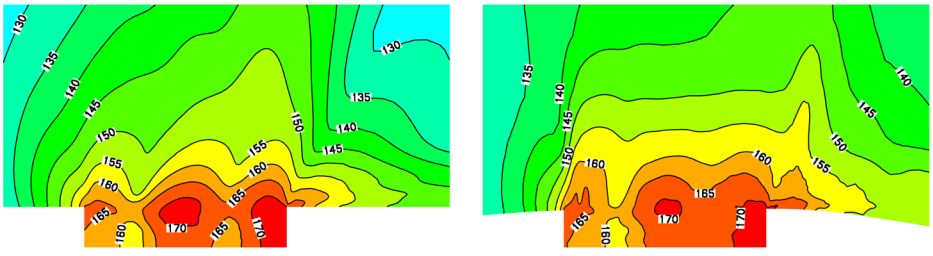

a) Ideal cavity b) UCAV cavity

Fig. 17 Contours of OASPL at the cavity centerline for the a) M219 cavity and b) empty UCAV cavity.

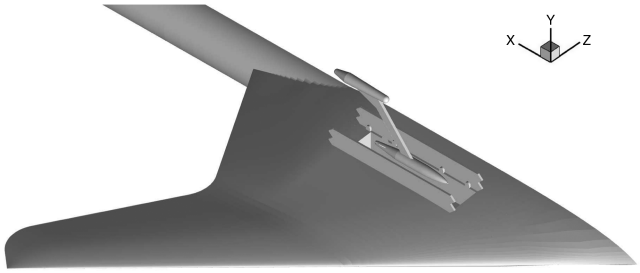

a) UCAV with cavity and store

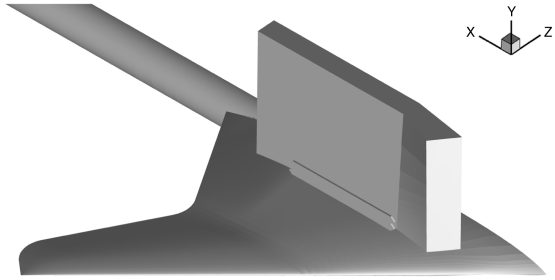

b) UCAV with sliding plane

Fig. 18 Geometry for the a) UCAV with cavity and store and b) surfaces of the sliding planes.

number was reduced to one million. This case has been compared to PIV data in previous studies [3,4]. Instantaneous isosurfaces of Q criteria [34] are shown in Fig. 16. The door hinges and the shape of the doors at the leading edge in the UCAV cavity generated large amounts of small structures, which makes a comparison between the two cases difficult. However, similar-sized structures existed inside the cavity region for both cases.

Although the grid in the far field was not designed for studying the acoustic field, the OASPL gives an idea of how the pressure waves propagate outside the cavity (Fig. 17). It can be seen that for the UCAV cavity, levels above 170 dB existed all across the aft wall and levels were in excess of 165 dB for the aft two-thirds of the cavity opening. Close to the front of the cavity, levels reduced to between 155 and 165 dB; however, at the area around the front lip of the cavity levels were above 165 dB. There are strong similarities to the idealized cavity case, especially in the front half of the cavity and around the aft wall. Outside the cavity, levels between 140 and 150 dB are seen approximately one cavity length above the cavity mouth. This is also very similar to the clean-cavity case.

B. Weapons Bay with Store

In the experiments, pressure measurements were taken with the store statically placed in four locations: inside the cavity, on the exit plane of the cavity, in the middle of the bay doors, and in the far field. Results presented here were from a computation of the UCAV with a store located between the doors of the cavity, where the apex of the store had a position of $y/L = 0.079$.

Figure 18a shows the geometry with the store placed between the doors. The extra store, sting, and force balance geometry would be complex to block alone, without the added difficulty of incorporating it into the already complex UCAV-cavity blocking. Therefore. to accommodate the store, sting, and force balance in the UCAV grid topology, sliding meshes were used [45]. The method involved installing surfaces into the UCAV grid that represented the sliding planes, then removing the sections of the grid inside the surfaces to

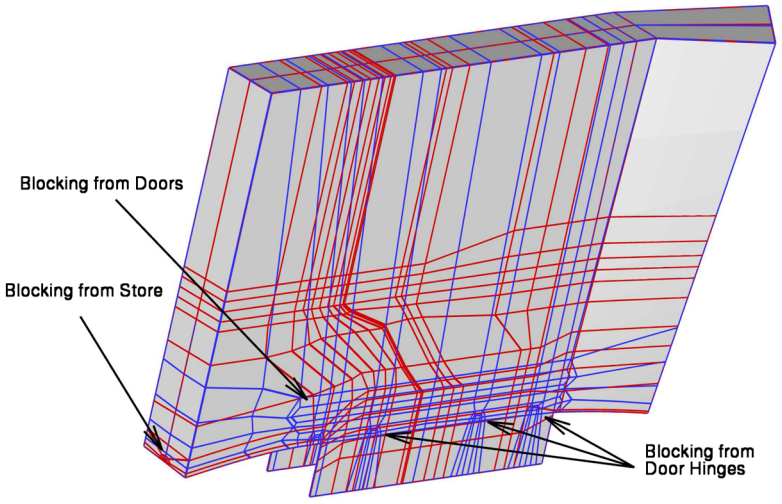

a) Boundaries of sliding plane

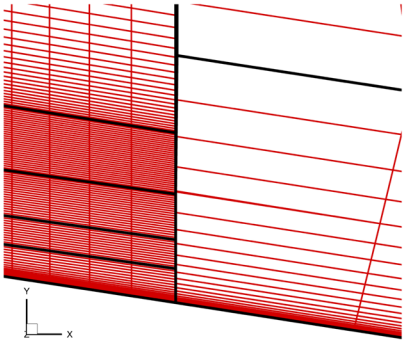

b) Cells at the boundary

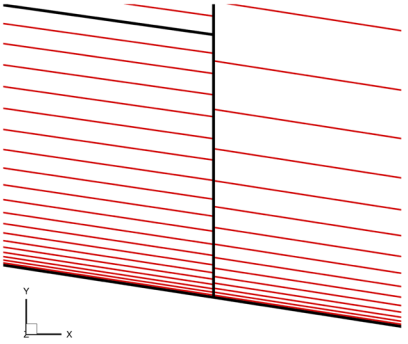

c) Cells at the surface

Fig. 19 Schematics showing the boundaries of the sliding-plane section from the a) UCAV grid and the store grid, b) matching cells close to the UCAV surface, and c) matching issues along sliding-plane boundary.

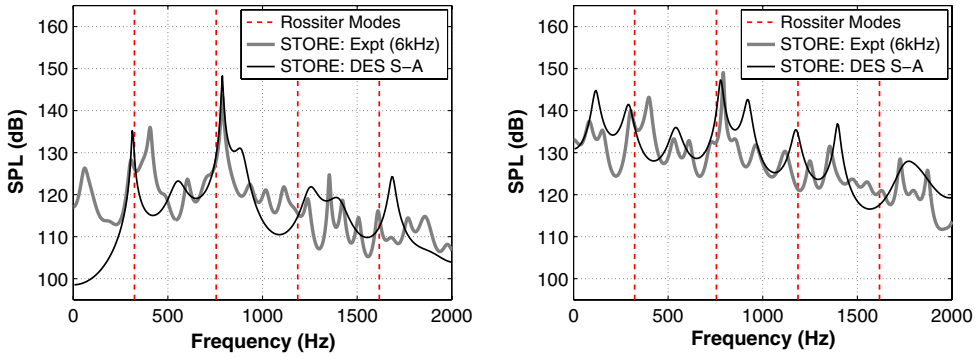

a) $x/L = 0.03$ b) $x/L = 0.92$

Fig. 20 PSD plots for the UCAV cavity with a store between the doors comparing results from computations to the experimental data from Hill and Lawson [22]: a) front and b) rear transducers on the cavity floor, presented in terms of SPL.

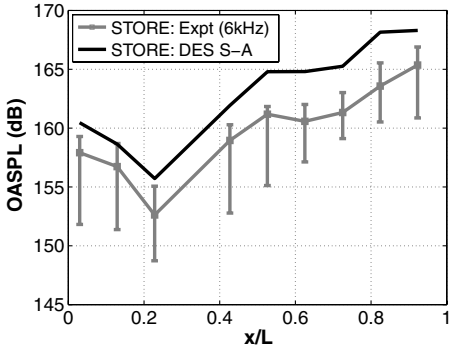

a) OASPL

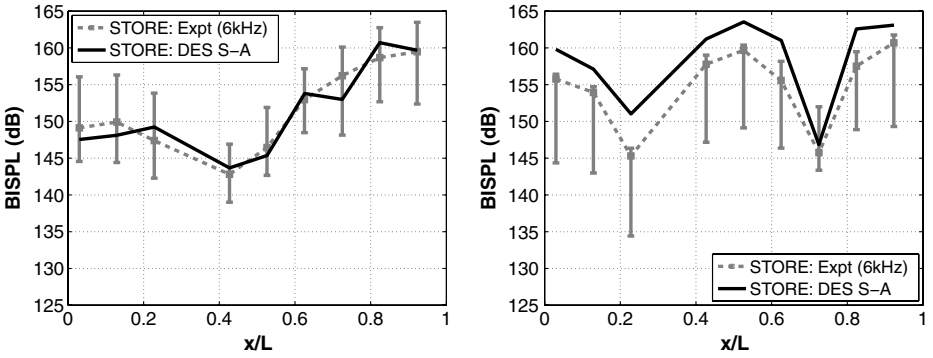

b) Mode 1: $200 \leqslant f \leqslant 400$ Hz c) Mode 2: $700 \leqslant f \leqslant 900$ Hz

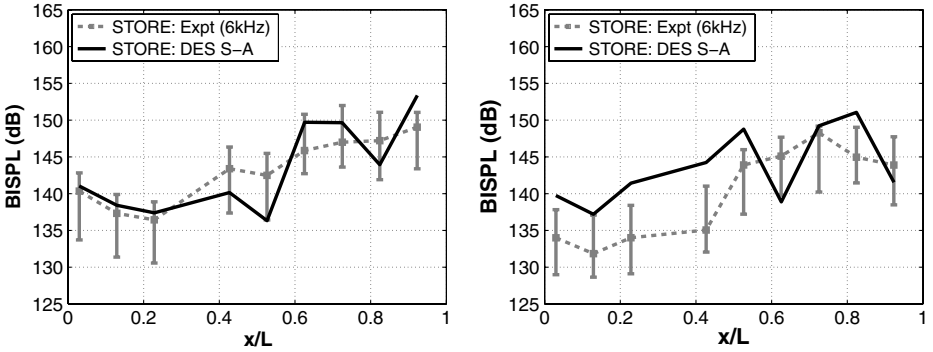

d) Mode 3: $1100 \leqslant f \leqslant 1300$ Hz e) Mode 4: $1500 \leqslant f \leqslant 1700$ Hz

Fig. 21 Plots of a) OASPL and b–e) BISPL along the cavity floor for the UCAV cavity with a store between the doors comparing results from computations to experimental data from Hill and Lawson [22]. The error bars denote minimum and maximum values from the different sections of the experimental data.

create a hole, into which a second grid that encompassed the store was inserted. The sliding-plane section, shown in Fig. 18b, was able to accommodate all store positions used in the experiments [22].

It should also be noted that the second grid extended the complete depth of the cavity and so the bottom of the grid was not a sliding plane, but the solid cavity surface. However, the was a gap between the sliding planes and cavity surfaces around the front, back, and sides. The cavity section of the grid contained 300 cells in length, 60 in width and 60 in depth, which gave the cavity section a total of 1.08 million cells. The removal of the sliding-plane section from the original UCAV grid [19–21] reduced the total number of cells from 12.4 to 10.5 million, while the second grid had a size of 7 million points. Although this is a large increase over the UCAV with cavity grid, it is much smaller than the grid would have been if an attempt was made to produce a blocking structure around the whole geometry in one. The blocking structure for the two grids on the sliding plane is shown in Fig. 19a, which illustrates that both blocking topologies were very complex and very different. This highlights the need for using the sliding-mesh technique in this scenario. However, as a consequence of the mesh refinement in the store part, matching the spacings between the cells on either side of the sliding plane had to be relaxed. Figures 19b and 19c show the mesh at the sliding-plane boundary for a slice in the streamwise direction.

The simulation was ran at the same Mach number as the empty-cavity computation; however, the added complexity from the addition of the store, sting, and force balance meant achieving a grid of high enough quality for a high Reynolds number computation was difficult. This was also problematic due to the inaccuracy of the initial CAD model. Therefore, it was decided to reduce the Reynolds number down to one million for this configuration.

The large size of the mesh and the use of the sliding-mesh method made this an expensive case to compute. The computation used approximately 74,000 CPU hours and has performed 8200 steps. After discarding the transient data, the signal length was approximately 0.01 s, equivalent to about three periods of the lowest Rossiter mode. Although this is a very short signal length, it can be analyzed to give an idea of the accuracy compared to the experiments. Note that no deliberate attempt was made to optimize the mesh size or sliding plane. Limited experiments also meant that a thorough assessment of DES was not possible.

The PSD spectra (Fig. 20) revealed that the second Rossiter mode was much more dominant than any other. The magnitude of the tones in both the front and rear of the cavity compared well to the experimental data, as did the frequency of the second mode. Although the frequency of the first mode was underpredicted, the comparisons were very encouraging, especially for such a complex geometry.

The OASPL and BISPL plots are shown in Fig. 21 and show the same trends as discussed in previous cases. The numerical results overpredicted the OASPL by 2–4 dB along the cavity floor. The levels within the first mode were very similar to the experiments and the second mode was slightly overpredicted. However, the shape of both the first two modes compared well to experimental curves. However, the same cannot be said for the third and fourth frequency bands. The experimental data did not show any identifiable tones for these modes and so were really just representative of the broadband noise. Even so, the levels were generally within the limits for the third band and overpredicted for the fourth.

Figure 22 shows isosurfaces for the cavity with store at the same Q level as presented for previous cases. Here, the vortical flow emanating from the center of the doors and the door hinges is still visible. In addition, small structures inside the cavity originated from the rear end and the fins of the store. Structures were also seen at the point where the sting attached to the store. The sting and force balance had a strong effect on the flow and vortex shedding was observed from the blunt trailing edge of the sting and the rear of the force balance.

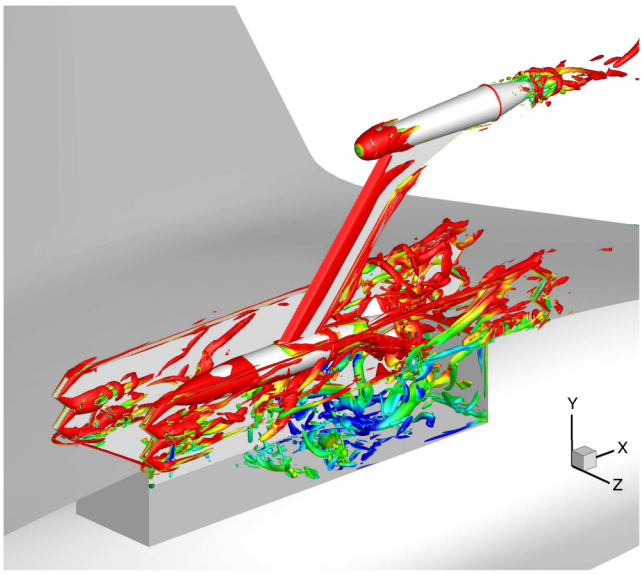

Fig. 22 Instantaneous isosurfaces of Q criteria for the UCAV cavity with a store between the doors. Isosurfaces at $Q = 2000$ are shown and shaded with streamwise velocity (nondimensionalized with respect to the freestream velocity), where levels are between -0.5 and $+0.5$.

C. Flowfield Comparisons

Instantaneous contours of Mach number are shown in Fig. 23 for the two UCAV configurations. The flowfields for the empty cavity were comparable to the M219 cavity with doors attached since oscillations of the shear layer close to the cavity leading edge could be identified and the wave structures were also produced. However, it appears that the motion of the shear layer was much more extreme in this case, since the displacement was almost the full depth of the cavity. This could be attributed to a few different aspects, including the increased flow velocity over the top of the cavity, the thinner upstream boundary layer and the fact that the UCAV body ahead of the cavity was not parallel to the freestream flow due to the aerodynamic shape used for the UCAV.

The addition of the store in between the doors had a major effect in reducing the oscillations of the shear layer. The boundary layer separated from the UCAV at the leading edge of the cavity as in the empty-cavity case; however, the store appeared to restrict the motion of the shear layer above the cavity opening. Downstream of the store apex, the thickness of the store deflected the shear layer down into the cavity. After the midpoint, the reduced thickness allowed the shear layer to oscillate, although at a much reduced level than in the empty-cavity configuration.

Figure 24 compares the averaged streamwise velocity profiles for the cases. The first profile ($x/L = 0.1$) for the empty UCAV cavity shows that the shear layer had diffused to a lesser degree and dipped into the cavity more than the M219 case. The same can be said for the second profile, where the averaged flow was equal to the freestream flow at the same level as the cavity opening. An interesting note is that the profiles for the store configuration were very similar to the empty-cavity configuration. At the third (cavity midpoint) and fourth profiles, the redirection of the shear layer by the store caused an increase in flow velocity compared to the empty cavity. Comparing the final three profiles of the UCAV configurations to the M219 cavity profiles, both UCAV configurations had a positive streamwise velocity further down into the cavity, revealing the increased diffusion of the shear layer.

The large oscillations of the shear layer in the empty cavity caused the center of the primary vortex to be located in the front half of the cavity, rather than in the rear. This allowed the shear layer to stay coherent into the cavity to a much higher degree than in the M219 cavity configuration. In the store configuration, the center of the primary vortex was located at slightly past the midpoint of the cavity. There was also a vortex in the front lower corner of the cavity, which was larger than the ones observed in the M219 cavity configurations.

The shear layer of the averaged flowfields can be further analyzed using the momentum thickness. However, since the flow velocity

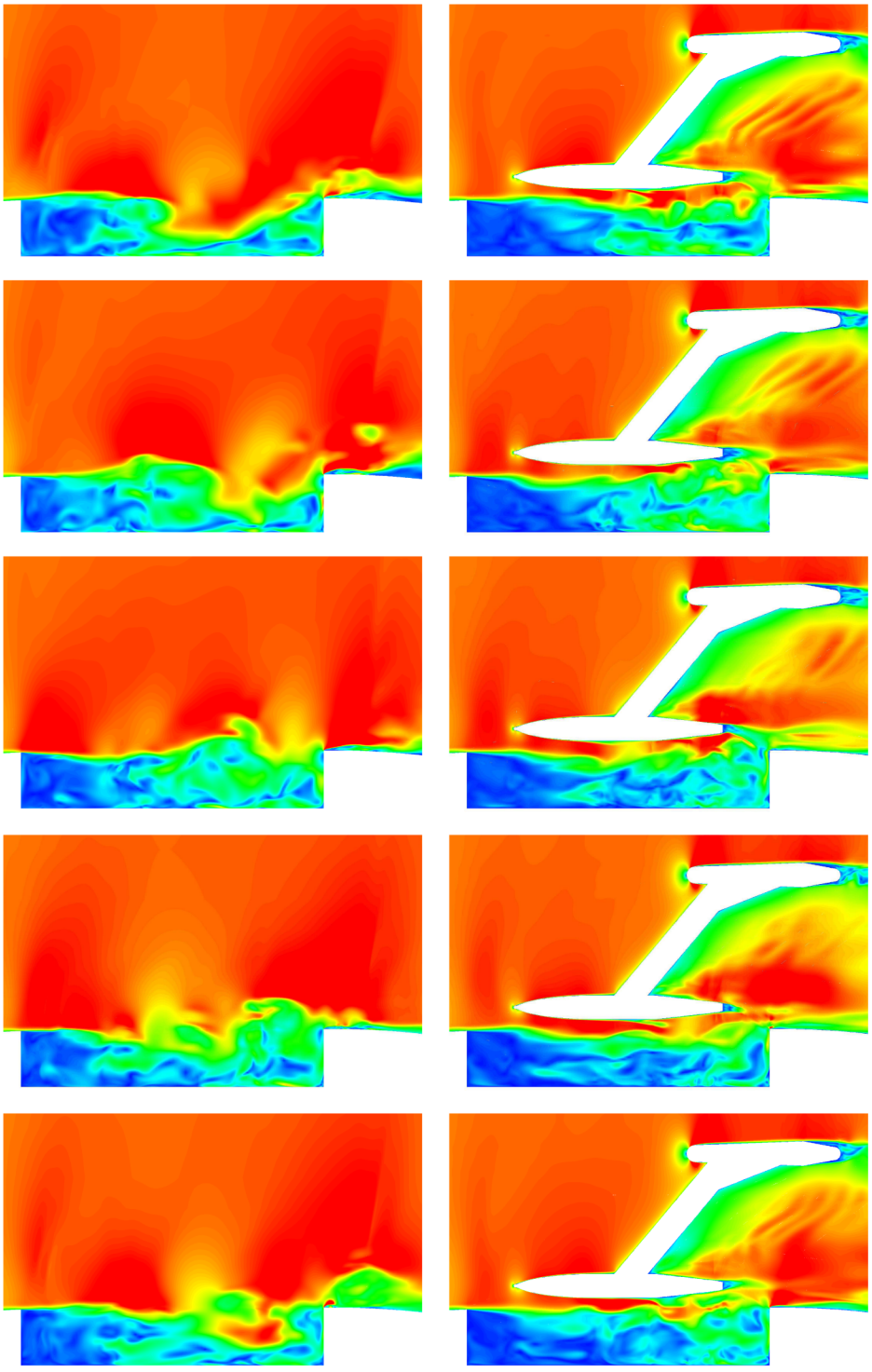

Fig. 23 Instantaneous contours of Mach number for the empty UCAV cavity (left column) and with a store between the doors (right column). Planes are located at the cavity centerline and Mach number levels range between 0 and 1.

over the top of the cavity was higher than the freestream velocity, the upper limit of the integral of the momentum thickness had to be altered. Instead of evaluating the integral to infinity (i.e., the far-field boundary), it was limited to the point where the flow velocity was equal to the freestream flow velocity. For the M219 case, it was observed that the doors caused a blocking effect and so gave high values of δ_m at the leading edge. Then the flow accelerating through the door opening caused a reduction in δ_m. Figure 25 shows that although the UCAV cavities had doors attached, the same behavior was not observed. The plot also shows the relatively thin boundary layer at the cavity leading edge for the UCAV configurations.

Close to the front edge of the cavities, the growth rates were similar for all configurations. However, after $x/L = 0.2$, different flow structures appeared. The growth of the shear layer for the store computation was halted due to the proximity with the store apex. The empty cavity appeared to follow a similar trend, which was assumed to be due to the location of the primary vortex. At this location, the thickness of the shear layer was actually less than in the M219 case. However, downstream of the vortex, the thickness increased at a higher rate (approximately 0.041) and ended up with a higher peak value. In the store configuration, the shear layer thickened at a much reduced rate while underneath the store, which then drastically

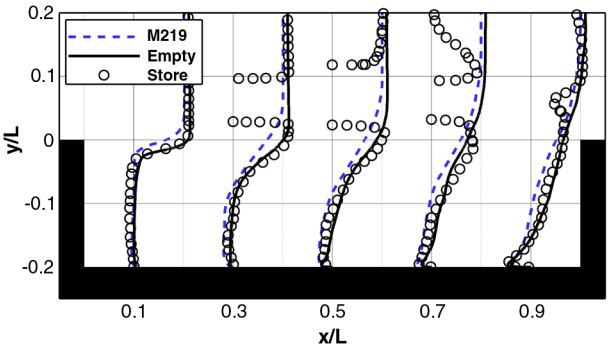

Fig. 24 Averaged streamwise velocity u profiles at the cavity centerline for the empty UCAV cavity and with a store in between the doors. Results are compared to the numerical results from the M219 clean cavity with doors attached.

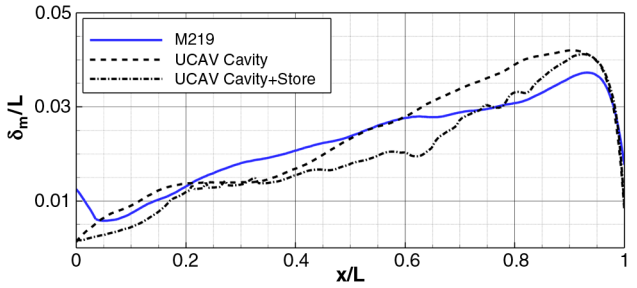

Fig. 25 Momentum thickness of the shear layer of the averaged empty UCAV cavity and with a store between the doors. Results are compared to the numerical results from the M219 clean cavity with doors attached. Momentum thickness is nondimensionalized by the cavity length.

increased in the final third of the cavity. Close to the aft wall, the peak value was actually similar to the empty cavity.

From the observation of the averaged momentum thickness, it appeared that the primary vortex in the empty-cavity configuration stabilized the flow, which can also be seen in plots of the turbulent kinetic energy (Fig. 26). Close to the front of the cavity ($x/L = 0.1$), the empty cavity had high levels of turbulent kinetic energy, with the store configuration having half the value. However, by $x/L = 0.2$, the kinetic energy had reduced in the empty cavity, while it increased in the M219 case. Levels for the first two profiles were very similar in the store configuration. These profiles also show the lower position in the normal direction of the shear layer for the UCAV configurations. Only by the cavity midpoint had the kinetic energy increased, for the UCAV cases, to higher levels than for the idealized case.

Although averaged plots in the streamwise direction show the influence of the store on the cavity dynamics, the influence in the spanwise direction is not as great. Figure 27 shows instantaneous contours of Mach number at the same time instants as in Fig. 23 for both the empty bay and with the store. Although the store is positioned so that it has little direct interaction with the shear layer, it is successful in reducing the oscillations, as already noted from the streamwise flowfields in Fig. 23. However, even with the large differences in the instantaneous flowfields, the averaged flowfields were much more similar. Figure 28 shows averaged contours at $x/L = 0.2$, 0.5 and 0.8. Note that the UCAV with an empty cavity

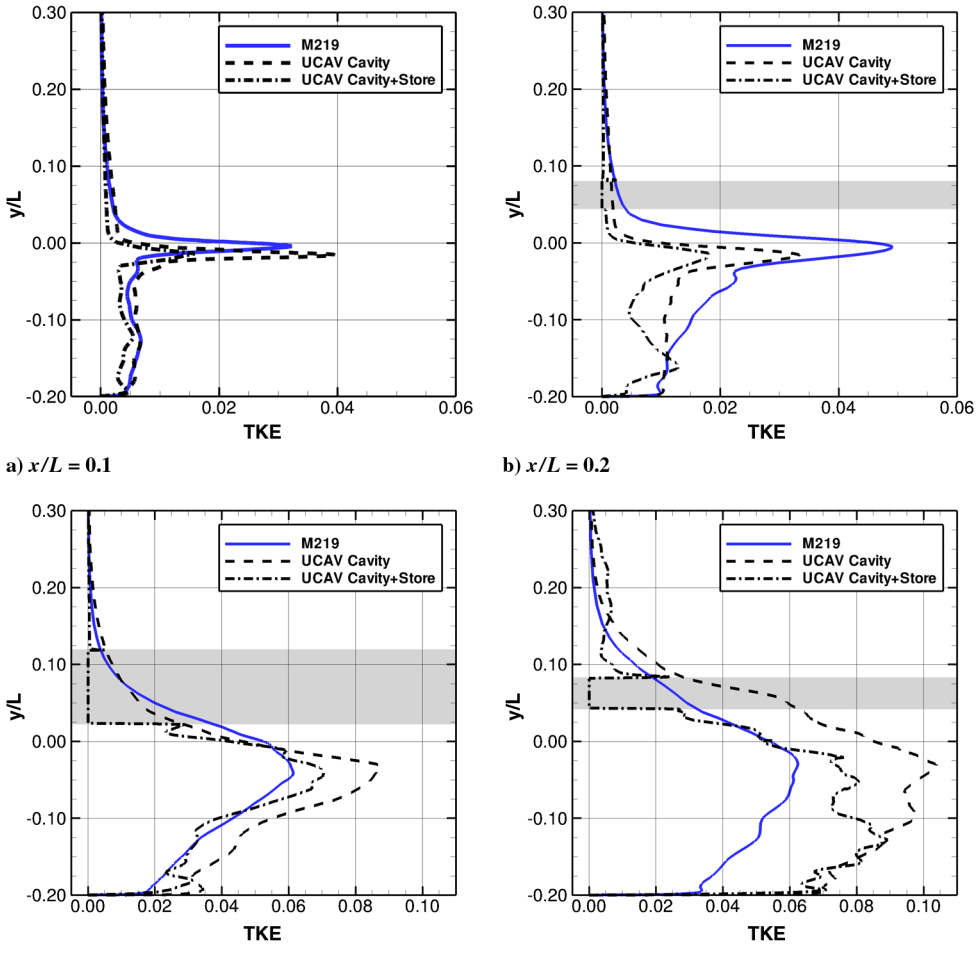

a) $x/L = 0.1$ **b) $x/L = 0.2$**

c) $x/L = 0.5$ **d) $x/L = 0.8$**

Fig. 26 Averaged turbulent kinetic energy profiles (k) at the cavity centerline for the empty UCAV cavity and with a store in between the doors. Results are compared to the numerical results from the M219 clean cavity with doors attached. Shaded areas indicate the location and thickness of the store.

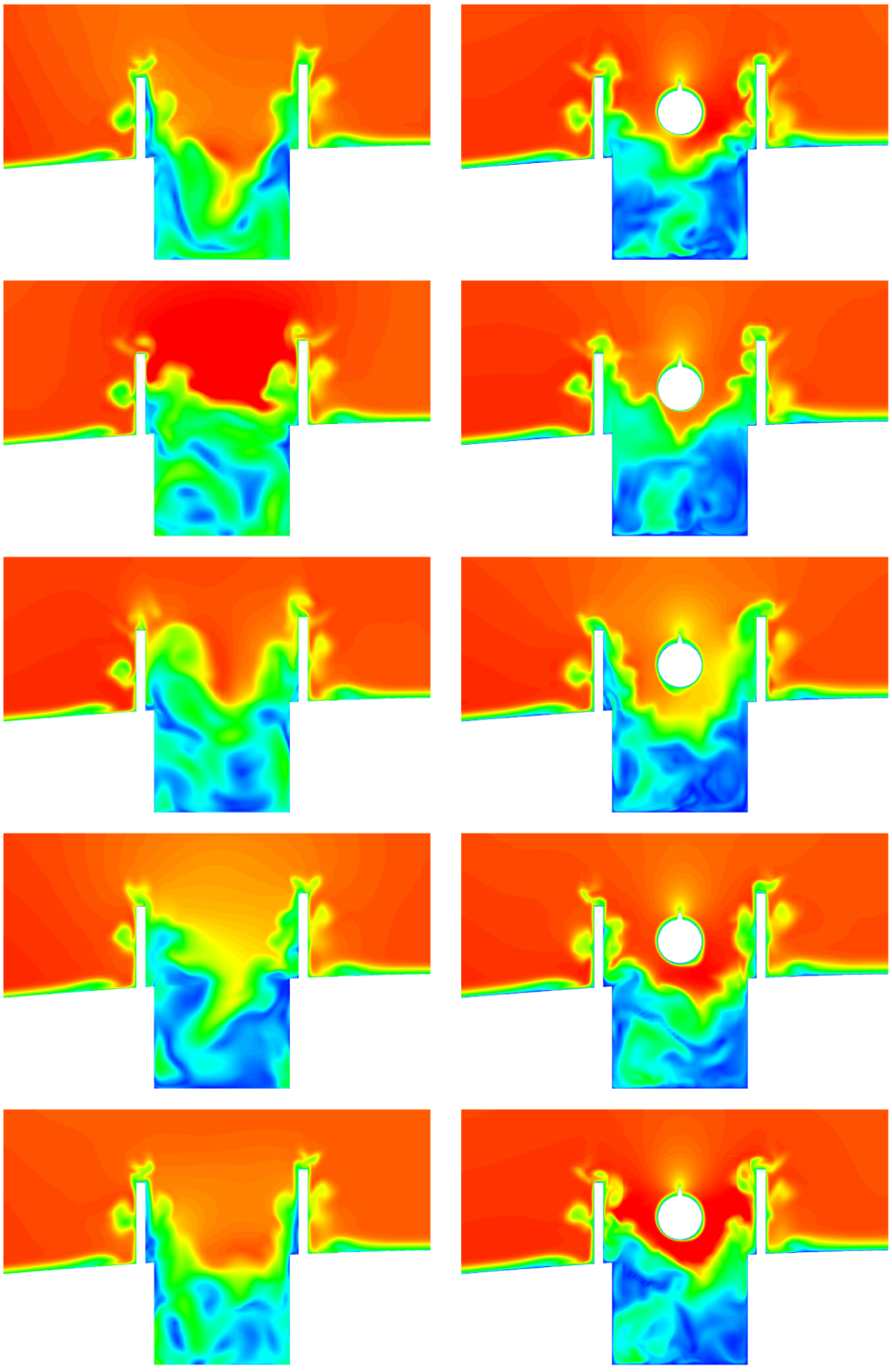

Fig. 27 Instantaneous contours of Mach number for the empty UCAV cavity (left column) and with a store between the doors (right column). Planes are located at $x/L = 0.5$ and Mach number levels range between 0 and 1.

was averaged over a longer duration than the configuration with the store. At all locations, the averaged flow on either side of the bay (such as the vortices created on the outside of the doors, the boundary layer on the UCAV surface and on the tops of the doors) is similar for both configurations. At $x/L = 0.2$, the vortices on the inside of the doors were more defined for the store configuration. The profile of the shear layer is similar, however, for both cases. At the second location, the Mach number above the store is lower since the position of the slice is just in front of the sting supporting the store. Again, the profile of the shear layer is similar to the empty UCAV configuration; however, the reduced averaging period for the store configuration is evident inside the cavity. At the final location, the fins on the store and a section of the sting supporting the store are visible. Although not shown in the plot, the force balance is above the section of the sting and so areas of high Mach number are visible on either side of the sting.

Finally, contours of OASPL at the cavity centerline revealed for the store configuration, the levels in the front of the cavity had a similar distribution to the empty cavity, although levels were 5 dB lower. High values appeared at the aft wall, but the area was much smaller than in the empty configuration. Outside the cavity, the OASPL was effected greatly by the sting and force balance and so a comparison with the empty cavity cannot be made. Even so, the values were much higher, especially ahead of the cavity. It appears that the store helped the shear layer to remain coherent and for this reason the midpart of the cavity shows low levels of OASPL.

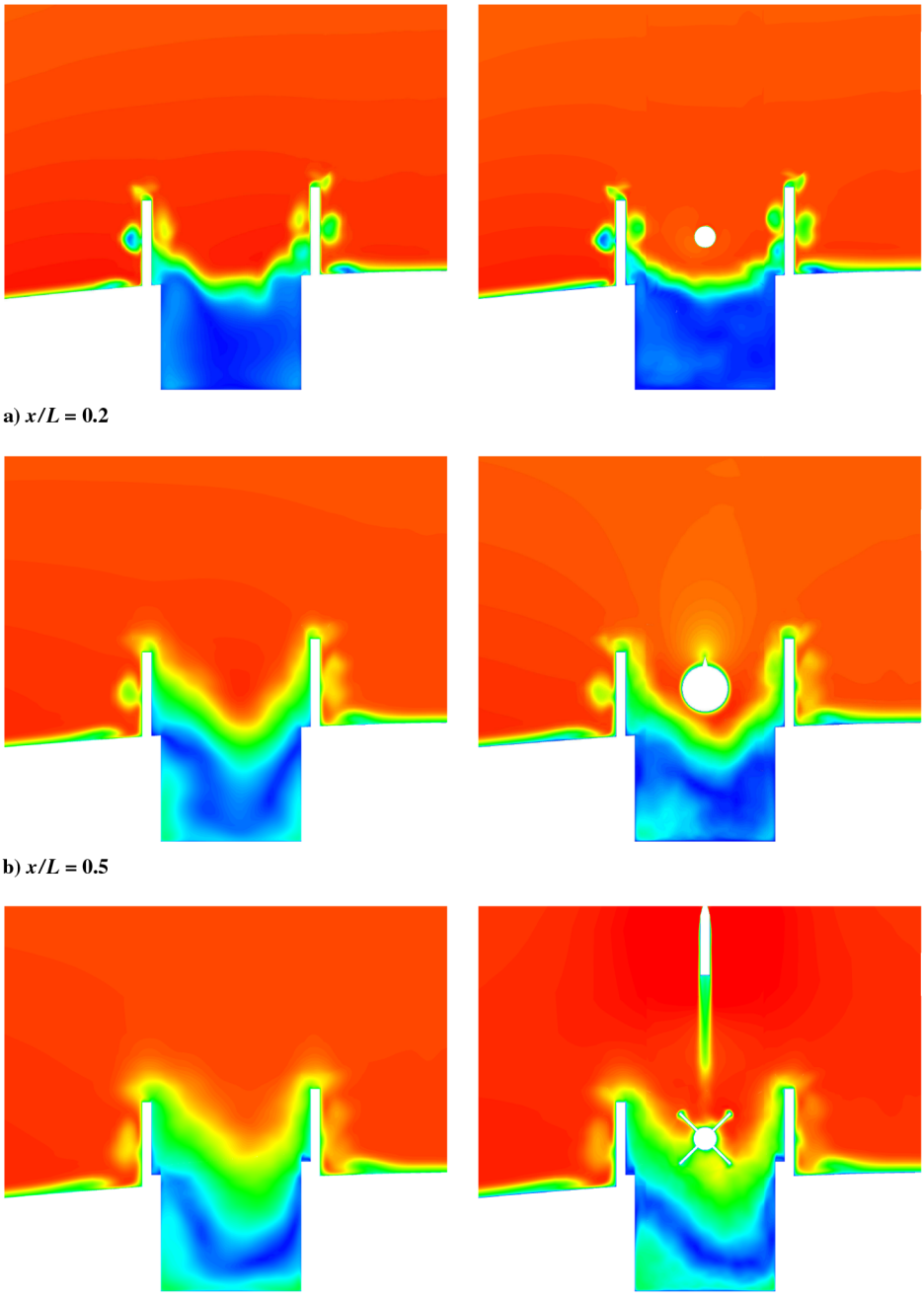

a) $x/L = 0.2$

b) $x/L = 0.5$

c) $x/L = 0.8$

Fig. 28 Averaged contours of Mach number for the empty UCAV cavity (left column) and with a store between the doors (right column). Mach number levels range between 0 and 1.

V. Conclusions

Results from computation have been presented with the aim of obtaining better comparisons with experimental data for flows in weapons bays. Methods employed (SEM and fluctuations from a precursor LES simulation) to increase the high-frequency content in the boundary layer upstream of the cavity suggested that since the inflow is important, the complete aircraft geometry should be studied. Instantaneous flowfields for computations with inflow forcing revealed the structure of the flow at the front of the cavity had a more three-dimensional nature and the properties of the shear layer (such as the shear-layer growth) were altered downstream. This was also reflected in the OASPL along the shear layer. Averaged profiles showed little change in the streamwise velocity; however, the profiles of normal velocity were noticeably different. These results suggest that the structure of the upstream boundary layer does affect the cavity flowfield, where the most encouraging sign was the reduction of the second Rossiter mode in the BISPL along the floor and shear layer. If the effect was similar on the results for computations using the M219 cavity, then the comparisons between numerical and experimental data would be more favorable.

For the computations of the full UCAV configuration, advanced multiblock topologies had to be used to properly represent the planform of the UCAV and all the details of the cavity, including doors and hinges, while sliding meshes were needed to insert the store. Computations with an empty cavity and with a store between the doors were carried out using the DES S-A model and comparisons to experimental data were very encouraging for such complex configurations. Visualizations using the Q criteria revealed the added turbulent content due to the door leading edges and the door hinges. Analysis of the shear layer showed an increase in oscillations, although this were restricted to the rear part of the cavity in both cases. For the empty cavity, the primary vortex was located in the front part of the cavity and this reduced the fluctuating components of

the velocities to lower values than in the idealized case. However, downstream of the primary vortex, the energy in the flow increased dramatically, causing the oscillations to extend almost the full depth of the cavity. This could be attributed to the reduced thickness of the boundary layer upstream and so less energy was initially contained within the shear layer, making it more likely to break down.

The addition of a store in between the doors had little effect close to the front wall. However, averaged flowfields showed that the proximity of the shear layer to the apex of the store deflected it downward into the cavity and restricted its growth. Further downstream, the influence of the store reduced and the shear layer thickened at a rate higher than in the empty case. Therefore, close to the aft wall was peak values was similar to the empty case. Outside the cavity, shedding was observed from the sting and force balance.

Acknowledgments

The financial support of the Engineering and Physical Sciences Research Council through grant EP/C533380/1 is gratefully acknowledged. The authors would like to extend their gratitude to Trevor Birch of the Defence Science and Technology Laboratory for providing the experimental data. The use of the HECToR system as part of the Second Applied Aerodynamics Consortium (U.K.) is also acknowledged.

References

[1] Rizzetta, D., and Visbal, M., "Large-Eddy Simulation of Supersonic Cavity Flow-Fields Including Flow Control," *AIAA Journal*, Vol. 41, No. 8, Aug. 2003, pp. 1452–1462. doi:10.2514/2.2128

[2] Larchevêque, L., Sagaut, P., Lê, T.-H., and Comte, P., "Large-Eddy Simulation of a Compressible Flow in a Three-Dimensional Open Cavity at High Reynolds Number," *Journal of Fluid Mechanics*, Vol. 516, 2004, pp. 265–301. doi:10.1017/S0022112004000709

[3] Nayyar, P., Barakos, G. N., and Badcock, K. J., "Numerical Study of Transonic Cavity Flows Using Large-Eddy and Detached-Eddy Simulation," *The Aeronautical Journal*, Vol. 111, No. 1117, March 2007, pp. 153–164.

[4] Barakos, G., Lawson, S., Steijl, R., and Nayyar, P., "Numerical Simulations of High-Speed Turbulent Cavity Flows," *Flow, Turbulence and Combustion*, Vol. 83, No. 4, Dec. 2009, pp. 569–585. doi:10.1007/s10494-009-9207-1

[5] Lawson, S., and Barakos, G., "Assessment of Passive Flow Control Devices for Transonic Cavity Flows Using Detached-Eddy Simulation," *Journal of Aircraft*, Vol. 46, No. 3, May–June 2009, pp. 1009–1029. doi:10.2514/1.39894

[6] Rossiter, J., "Wind Tunnel Experiments on the Flow Over Rectangular Cavities at Subsonic and Transonic Speeds," Royal Aircraft Establishment, TR 64037, London, Oct. 1964.

[7] Sagaut, P., Garnier, E., Tromeur, E., Larchevêque, L., and Labourasse, E., "Turbulent Inflow Conditions for Large-Eddy Simulation of Compressible Wall-Bounded Flows," *AIAA Journal*, Vol. 42, No. 3, March 2004, pp. 469–477. doi:10.2514/1.3461

[8] Lee, S., Lele, S., and Moin, P., "Simulation of Spatially Evolving Turbulence and the Application of Taylor's Hypothesis in Compressible Flow," *Physics of Fluids A*, Vol. 4, No. 7, July 1992, pp. 1521–1530. doi:10.1063/1.858425

[9] Keating, A., Piomelli, U., Balaras, E., and Kaltenbach, H.-J., "A Priori and Posteriori Tests of Inflow Conditions for Large–Eddy Simulation," *Physics of Fluids*, Vol. 16, No. 12, Dec. 2004, pp. 4696–4712. doi:10.1063/1.1811672

[10] Lund, T., Wu, X., and Squires, K., "Generation of Turbulent Inflow Data for Spatially-Developing Boundary Layer Simulations," *Journal of Computational Physics*, Vol. 140, No. 2, March 1998, pp. 233–258. doi:10.1006/jcph.1998.5882

[11] Ferrante, A., and Elghobashi, S., "A Robust Method for Generating Inflow Conditions for Direct Simulations of Spatially-Developing Turbulent Boundary Layers," *Journal of Computational Physics*, Vol. 198, 2004, pp. 372–387. doi:10.1016/j.jcp.2004.01.016

[12] Batten, P., Goldberg, U., and Chakravarthy, S., "Interfacing Statistical Turbulence Closures with Large—Eddy Simulation," *AIAA Journal*, Vol. 42, No. 3, March 2004, pp. 485–492. doi:10.2514/1.3496

[13] Jarrin, N., Benhamadouche, S., Laurence, D., and Prosser, R., "A Synthetic-Eddy Method for Generating Inflow Conditions for Large-Eddy Simulations," *International Journal of Heat and Fluid Flow*, Vol. 27, 2006, pp. 585–593. doi:10.1016/j.ijheatfluidflow.2006.02.006.

[14] Jarrin, N., Uribe, J.-C., Prosser, R., and Laurence, D., "Synthetic Inflow Boundary Conditions for Wall Bounded Flows," *Advances in Hybrid RANS-LES Modelling*, Notes on Numerical Fluid Mechanics and Multidisciplinary Design, Vol. 97, Springer, Berlin, 2008, pp. 77–86. doi:10.1007/978-3-540-77815-8

[15] Pamiès, M., Weiss, P.-É., Garnier, E., Deck, S., and Sagaut, P., "Generation of Synthetic Turbulent Inflow Data for Large Eddy Simulation of Spatially Evolving Wall-Bounded Flows," *Physics of Fluids*, Vol. 21, 2009. doi:10.1063/1.3103881.

[16] Gloerfelt, X., Bogey, C., and Bailly, C., "LES of the Noise Radiated by a Flow over a Rectangular Cavity," *Proceedings of the International Workshop on LES for Acoustics*, DLR, German Aerospace Center, Gottingen, Germany, 7–8 Oct. 2002, 2002.

[17] Chang, K., Constantinescu, G., and Park, S.-O., "Assessment of Predictive Capabilities of Detached Eddy Simulation to Simulate Flow and Mass Transport Past Open Cavities," *Journal of Fluids Engineering*, Vol. 129, Nov. 2007, pp. 1372–1383. doi:10.1115/1.2786529

[18] Wong, M., McKenzie, G., Ol, M., Petterson, K., and Zhang, S., "Joint TTCP CFD Studies into the 1303 UCAV Performance: First Year Results," 24th AIAA Applied Aerodynamic Conference, San Francisco, AIAA Paper 2006-2984, June 2006.

[19] Lawson, S., and Barakos, G., "DES for UCAV Weapon Bay Flow," *Proceedings of the Third Symposium on Hybrid RANS-LES Methods*, Gdansk, Poland, 10–12 June, 2009.

[20] Lawson, S., and Barakos, G., "Evaluation of DES for Flows Around UCAVs," *Proceedings of the CEAS 2009 European Air and Space Conference*, Manchester, England, U.K., 26–29 Oct. 2009.

[21] Lawson, S. J., and Barakos, G. N., "Evaluation of DES for Weapons Bays in UCAVs," *Aerospace Science and Technology* (to be published). doi:10.1016/j.ast.2010.04.006

[22] Hill, A., and Lawson, S., "Tests Conducted in the ARA 2.74 m × 2.44 m Transonic Wind Tunnel on the Release of a Generic MK82/GBU-30 JDAM Store Model from a Generic UCAV Model Using the ARA Two Sting Rig," Aircraft Research Association, Bedford, England, U.K., Nov. 2004.

[23] Badcock, K., Richards, B., and Woodgate, M., "Elements of Computational Fluid Dynamics on Block Structured Grids Using Implicit Solvers," *Progress in Aerospace Sciences*, Vol. 36, Nos. 5–6, July 2000, pp. 351–392. doi:10.1016/S0376-0421(00)00005-1

[24] Osher, S., and Chakravarthy, S., "Upwind Schemes and Boundary Conditions with Applications to Euler Equations in General Geometries," *Journal of Computational Physics*, Vol. 50, 1983, pp. 447–481. doi:10.1016/0021-9991(83)90106-7

[25] Roe, P., "Approximate Riemann Solvers, Parameter Vectors and Difference Schemes," *Journal of Computational Physics*, Vol. 43, 1981, pp. 357–372. doi:10.1016/0021-9991(81)90128-5

[26] Van Leer, B., "Towards the Ultimate Conservative Conservative Difference Scheme II: Monotonicity and Conservation Combined in a Second Order Scheme," *Journal of Computational Physics*, Vol. 14, 1974, pp. 361–374. doi:10.1016/0021-9991(74)90019-9

[27] Jameson, A., "Time Dependent Calculations Using Multigrid, with Applications to Unsteady Flows Past Airfoils and Wings," 10th AIAA Computational Fluid Dynamics Conference, Honolulu, 1991, AIAA Paper 1991-1596.

[28] Eisenstat, S., Elman, H., and Schultz, M., "Variational Iterative Methods for Nonsymmetric Systems of Linear Equations," *SIAM Journal on Numerical Analysis*, Vol. 20, No. 2, 1983, pp. 345–357. doi:10.1137/0720023

[29] Childers, D. (ed.)., *Modern Spectrum Analysis*, IEEE Press, New York, 1978, Chap. 2, pp. 23–148.

[30] Pierce, A., *Acoustics: An Introduction to Its Physical Principles and Applications*, Acoustical Society of America, Woodbury, NY, 1989.

[31] Heller, H., Holmes, D., and Covert, E., "Flow Induced Pressure Oscillations in Shallow Cavities," *Journal of Sound and Vibration*, Vol. 18, No. 4, Oct. 1971, pp. 545–553; also U.S. Air Force Flight Dynamics Lab. TR-70-104, Wright-Patterson AFB, OH, Dec. 1970.

doi:10.1016/0022-460X(71)90105-2
[32] Browand, F., and Troutt, T., "The Turbulent Mixing Layer: Geometry of Large Vortices," *Journal of Fluid Mechanics*, Vol. 158, 1985, pp. 489–509.
doi:10.1017/S0022112085002737
[33] Huang, L.-S., and Ho, C.-M., "Small-Scale Transition in a Plane Mixing Layer," *Journal of Fluid Mechanics*, Vol. 210, 1990, pp. 475–500.
doi:10.1017/S0022112090001379
[34] Hunt, J., Wray, A., and Moin, P., "Eddies, Streams and Convergence Zones in Turbulent Flows," *Proceedings of the Summer Program*, Center for Turbulence Research, Stanford, CA, 1988, pp. 193–207.
[35] Jeong, J., and Hussain, F., "On the Identification of a Vortex," *Journal of Fluid Mechanics*, Vol. 285, 1995, pp. 69–94.
doi:10.1017/S0022112095000462
[36] Barakos, G. N., Lawson, S. J., Steijl, R., and Nayyar, P., "Assessment of Flow Control Devices for Transonic Cavity Flow Using DES and LES," *IUTAM Symposium on Unsteady Separated Flows and Their Control*, IUTAM Bookseries, Vol. 14, Springer, Amsterdam, 2009, pp. 77–87.
doi:10.1007/978-1-4020-9898-7_7
[37] Lawson, S. J., Barakos, G. N., and Nayyar, P., "Appendix for Test Case A2—M219 Cavity Flow: Computations with and Without Bay Doors," *DESider—A European Effort on Hybrid RANS-LES Modelling, Results of the European-Union Funded Project, 2004–2007*, Notes on Numerical Fluid Mechanics and Multidisciplinary Design, Vol. 103, Annex 18A, Springer, Berlin, 2009.
doi:10.1007/978-3-540-92773-0
[38] Lawson, S. J., Barakos, G. N., and Simpson, A., "Understanding Cavity Flows Using Proper Orthogonal Decomposition and Signal Processing," *Journal of Algorithms & Computational Technology*, Vol. 4, No. 1, March 2010, pp. 47–70.
doi:10.1260/1748-3018.4.1.47
[39] Nightingale, D., Ross, J., and Foster, G., "Cavity Unsteady Pressure Measurements—Examples from Wind-Tunnel Tests," Ver. 3, QinetiQ, Aerodynamics & Aeromechanics Systems Group, Farnborough, England, U.K., Nov. 2005.
[40] Spalart, P., Jou, W.-H., Strelets, M., and Allmaras, S., "Comments on the Feasibility of LES for Wings, and on a Hybrid RANS/LES Approach," *Proceedings of the 1st AFOSR International Conference on DNS/LES*, Columbus, OH, Aug. 1997.
[41] Deck, S., Weiss, P.-É., Pamiès, M., and Garnier, E., "On the Use of Stimulated Detached Eddy Simulation (SDES) for Spatially Developing Boundary Layers," *Advances in Hybrid RANS-LES Modelling*, Notes on Numerical Fluid Mechanics and Multidisciplinary Design, Vol. 97, Springer, Berlin, 2008, pp. 67–76.
[42] Lin, J.-C., and Rockwell, D., "Organized Oscillations of Initially Turbulent Flow Past a Cavity," *AIAA Journal*, Vol. 39, No. 6, June 2001, pp. 1139–1151.
doi:10.2514/2.1427
[43] Bruce, R., and Mundell, A., "Low Speed Wind Tunnel Tests on the 1303 UCAV Concept," QinetiQ, TR QINETIQ/FST/TR025502/1.0, Farnborough, England, U.K., March 2003.
[44] Kegerise, M., Spina, E., Garg, S., and Cattafesta, L., III., "Mode-Switching and Nonlinear Effects in Compressible Flow over a Cavity," *Physics of Fluids*, Vol. 16, No. 3, March 2004, pp. 678–686.
doi:10.1063/1.1643736
[45] Steijl, R., and Barakos, G., "Sliding Mesh Algorithm for CFD Analysis of Helicopter Rotor-Fuselage Aerodynamics," *International Journal for Numerical Methods in Fluids*, Vol. 58, No. 5, Oct. 2008, pp. 527–549.
doi:10.1002/fld.1757